

Gravitational microlensing of γ -ray blazars

Diego F. Torres¹, Gustavo E. Romero^{2, 3}, Ernesto F. Eiroa⁴,
Joachim Wambsganss⁵, and Martín E. Pessah⁶

¹ *Physics Department, Princeton University, NJ 08544, USA*

² *Instituto Argentino de Radioastronomía (IAR), C.C. 5, 1894 Villa Elisa, Buenos Aires, Argentina*

³ *Max-Planck-Institute für Kernphysik, Postfach 103980, D-69029 Heidelberg, Germany*

⁴ *Instituto de Astronomía y Física del Espacio, C.C. 67, Suc. 28, 1428, Buenos Aires, Argentina*

⁵ *Universität Potsdam, Institut für Physik, Am Neuen Palais 10, 14469 Potsdam, Germany*

⁶ *Steward Observatory, University of Arizona, AZ 85721, USA*

1 November 2018

ABSTRACT

We present a detailed study of the effects of gravitational microlensing on compact and distant γ -ray blazars. These objects have γ -ray emitting regions which are small enough as to be affected by microlensing effects produced by stars lying in intermediate galaxies. We compute the gravitational magnification taking into account effects of the lensing and show that, whereas the innermost γ -ray spheres can be significantly magnified, there is little magnification either for very high γ -ray energies or for lower (radio) frequencies (because these wavelengths are emitted from larger regions). We analyze the temporal evolution of the gamma-ray magnification for sources moving in a caustic pattern field, where the combined effects of thousands of stars are taken into account using a numerical technique. We propose that some of the unidentified γ -ray sources (particularly some of those lying at high galactic latitude whose gamma-ray statistical properties are very similar to detected γ -ray blazars) are indeed the result of gravitational lensing magnification of background undetected Active Galactic Nuclei (AGNs). This is partly supported from a statistical point of view: we show herein as well, using the latest information from the Third EGRET Catalog, that high-latitude γ -ray sources have similar averaged properties to already detected γ -ray AGNs. Some differences between both samples, regarding the mean flux level, could also be understood within the lensing model. With an adequate selection of lensing parameters, it is possible to explain a variety of γ -ray light curves with different time scales, including non-variable sources. The absence of strong radio counterparts could be naturally explained by differential magnification in the extended source formalism. The spectral evolution of the sources during microlensing events is calculated, revealing specific features that can be used to test the models with the next generation of both, orbital and ground-based γ -ray telescopes.

Keywords: gamma-rays: observations, gamma-rays: theory, gravitational lensing, galaxies: active

1 INTRODUCTION

The first extragalactic γ -ray source detected was the quasar 3C273, which was observed by the COS-B satellite in a particularly active state in the 1970s (Swanenburg et al. 1978). Since then, many Active Galactic Nuclei (AGNs) have been detected at high energies, most of them belonging to the blazar class (e.g. Mukherjee 2001). The Third EGRET Catalog of point-like sources lists currently 67 detections labeled as AGNs (Hartman et al. 1999). Notwithstanding, a large number of γ -ray sources, scattered along the entire

sky, remain unidentified at present.

The unidentified γ -ray sources at low latitudes are probably related to several distinct galactic populations (Romero 2001). Among them there might be pulsars (e.g. Kaspi et al. 2000, Zhang et al. 2000, Torres et al. 2001d; Camilo et al. 2001; D’Amico et al. 2001), SNRs in interaction with molecular clouds (Combi & Romero 1995, Sturmer et al. 1996; Esposito et al. 1996; Combi et al. 1998; Combi et al. 2001, Butt et al. 2001, Torres et al. 2002b), stellar-size black holes (Punsly 1998a,b; Punsly et

al. 2000), X-ray transients (Romero et al. 2001), persistent microquasars (Paredes et al. 2000, Kaufman Bernadó et al. 2002), and massive stars with strong stellar winds (Benaglia et al. 2001). Some of these kinds of stellar objects present statistical positional correlation with unidentified EGRET sources (far from what is expected as a random result, e.g. Romero et al. 1999, Torres et al. 2001b). Pulsars, however, remain as the only confirmed low-latitude population, since pulsed γ -ray radiation has been already detected for at least six different sources (Thompson et al. 1999, Thompson 2001; Kaspi et al. 2000), five of them included in the Third EGRET Catalog (Hartman et al. 1999).

Gehrels et al. (2000) have shown that the mid-latitude sources are different from the bright population of unidentified sources along the Galactic plane. Some of the detections ($5^\circ < |b| < 30^\circ$) are thought to be associated with the Gould Belt (Grenier 2000, Gehrels et al. 2000), a starburst region lying at ~ 600 pc from Earth. Few other sources, at higher latitudes, could be the result of electrons being accelerated at the shock waves of forming clusters of galaxies (Totani & Kitayama 2000). However, for many of the high-latitude sources, no other explanation seems to be available than they are AGNs yet undetected at lower energies. This is particularly clear when one looks at the variability levels of the associated light curves: models requiring large acceleration region, like clusters of galaxies, would produce non-variable sources, contrary to what is found for most of the high latitude sources.

All identified 67 EGRET AGNs are also strong radio sources with flat spectra, as expected from synchrotron jet-like sources where the γ -ray flux is the result of inverse Compton scattering (Mattox et al. 1997). However, no strong radio source appears within the contours of the unidentified high latitude EGRET sources. In this paper, we shall develop a model, briefly outlined by Torres et al. (2002a), which focuses precisely on that difference and provides an explanation of why some of the high latitude unidentified sources might not be detected at low frequencies. *The main feature of such a model is that it will account for the γ -ray properties of the high latitude gamma-ray detections resorting to differential gravitational lensing magnification of background, high-redshift, AGNs with otherwise undetected γ -ray emission. Since these objects have different sizes at different wavelengths, differential microlensing effects will lead to a magnification of the innermost γ -ray emitting regions, whereas the radio emission will be largely unmagnified, therefore remaining under the detection threshold.*

The gravitational light deflection effect by compact objects on background sources is commonly called microlensing (e.g. Paczyński 1986). A source would be affected by different magnifications, depending on its position. Typically, source, lens, and observer move relative to each other, and therefore, this translates into a variable flux measured for the background source. Observationally, there are two interesting regimes of microlensing. Local

microlensing deals with the light deflection effects by stars inside the Milky Way disk on stars in the Galactic bulge. Here the probability for a microlensing event is of order $\times 10^{-6}$. This means that it is necessary to monitor millions of stars in order to see a few occurrences. But despite this small probability, various teams have been very successful in detecting this kind of events in recent years (for a review, see Paczyński 1996). The other interesting regime of microlensing is usually called quasar microlensing, but it can be applied to any other compact source at moderate to high redshift. In this case, an intervening galaxy provides the surface mass density in stars (or other compact objects) which act as microlenses on the background quasar (for a review, see Wambsganss 2001). Recently, this kind of microlensing has been suggested for other astrophysical sources as well, e.g. gamma-ray bursts (Williams & Wijers 1997), gamma-ray burst afterglows (Garnavich, Loeb & Stanek 2000; Mao & Loeb 2001; Koopmans & Wambsganss 2001), and superluminal shocks in extragalactic radio sources (Romero et al 1995, Koopmans & de Bruyn 2000). The gamma-ray sources discussed here are another type of astrophysical objects for which microlensing possibly plays an important role.

We recall that gravitational light deflection is basically an achromatic phenomenon, being a geometric effect predicted by General Relativity, i.e. the deflection angle does not depend on the energy of the photon. However, it is nevertheless possible to have chromaticity effects when the size of the source changes with the observing wavelength. A large source is typically less affected by a microlensing magnification than a small source (Wambsganss & Paczyński 1991). This size-induced chromaticity will be an essential ingredient of our model.

The structure of the paper is as follows. In Section 2 we present a statistical study of the main characteristics of the sample of unidentified γ -ray sources at high latitudes, including variability. In Section 3 we review the formalism for extragalactic gravitational microlensing in both the point-like and extended source cases. Section 4 comments on the inner structure of γ -ray emitting AGNs considered here as background sources. Section 5 contains our results for the flux and spectral evolution of single microlensing events in a variety of situations and different types of host galaxies. Section 6 deals with the optical depth problem and the expected number of microlensing events. Section 7 presents our results for full numerical modeling of caustic patterns for different galactic lensing parameters. Precise predictions for the light curves at different frequencies are also shown there. We finally close with some concluding remarks in Section 8.

2 UNIDENTIFIED γ -RAY SOURCES AT HIGH LATITUDES

2.1 Sample and photon spectral index

Previous population studies using the Second EGRET Catalog have already remarked that part of the sample

of high latitude unidentified sources is consistent with an isotropic population, a fact that supports an extragalactic origin for these detections (Özel & Thompson 1996). In what follows, we shall make a comparison between the properties of identified γ -ray AGNs in the Third EGRET Catalog and high-latitude unidentified sources. We shall choose the lower cut-off in latitude as $|b| = 30^\circ$, in order to avoid possible contamination from Gould Belt sources. There are 45 3EG unidentified sources within this latitude range; we provide details on these sources in Table 1.

Figure 1 shows the distribution of the γ -ray photon spectral index for both sets of sources, 45 unidentified EGRET sources and 67 detected EGRET AGNs. The mean value of the photon index is 2.36 ± 0.36 for AGNs, and 2.49 ± 0.34 for the unidentified detections. They are compatible within the uncertainties and, on average, steeper than what is observed for low latitude sources, which are thought to belong to our own Galaxy.

2.2 Variability

The study of the time variability of γ -ray sources is of fundamental importance. Several models for γ -ray sources in our Galaxy predict non-variable emission during the time scale of EGRET observations. AGNs, on the contrary, are expected to present a variable flux emission. Variability is, in case we were able to quantify it with some degree of precision, a powerful tool to probe the nature of the sources. Visual inspection of the flux evolution through the different viewing periods is obviously a first indication of the variability status of any given source. However, fluxes are usually the result of only a handful of incoming photons, experimental errors are sometimes huge and their origin uncertain, and consequently more reliable ways of quantizing the flux evolution should be devised: these are known as variability indices. Two such indices have been recently introduced in the literature and applied to 3EG sources so far (Tompkins 1999 (index τ), Torres et al. 2001a (index I)). In general, statistical results from these two indices are well correlated (see Torres et al. 2001c for a discussion). Here we shall adopt the index I , previously used in blazar variability analysis (Romero et al. 1995) and applied to some of the 3EG sources by Zhang et al. (2000) and Torres et al. (2001a,c) as our main quantitative evaluation of variability, although the results for τ are also given in Table 1. The basic idea behind the index I is to directly compare the flux variation of any given source with that shown by known γ -ray pulsars, which are assumed to be an intrinsically non-variable population. This index, contrary to Tompkins' index τ (Tompkins 1999), uses only the publicly available data of the 3EG Catalog.

Let us recall the basic elements that are used to define the I -index. Firstly, a mean weighted value for the EGRET flux is computed:

$$\langle F \rangle = \left[\sum_{i=1}^{N_{\text{vp}}} \frac{F(i)}{\epsilon(i)^2} \right] \times \left[\sum_{i=1}^{N_{\text{vp}}} \frac{1}{\epsilon(i)^2} \right]^{-1}, \quad (1)$$

where N_{vp} is the number of single viewing periods, $F(i)$ the observed flux in the i^{th} -period, and $\epsilon(i)$ the corresponding error. For those observations in which the significance (\sqrt{TS} in the EGRET catalog) is greater than 2σ , the error is $\epsilon(i) = F(i)/\sqrt{TS}$. For those observations which are in fact upper bounds on the flux, it is assumed that both $F(i)$ and $\epsilon(i)$ are half the value of the upper bound. The fluctuation index μ is defined as:

$$\mu = 100 \times \sigma_{\text{sd}} \times \langle F \rangle^{-1}. \quad (2)$$

In this expression, σ_{sd} is the standard deviation of the flux measurements. This fluctuation index is also computed for the confirmed γ -ray pulsars in the 3EG catalog, assuming the physical criterion that pulsars are non-variable γ -ray sources. The averaged statistical index of variability, I , is then given by the ratio

$$I = \frac{\mu_{\text{source}}}{\langle \mu \rangle_{\text{pulsars}}}. \quad (3)$$

Once the index is defined, we need to clarify the thresholds for variability. Following Torres et al. (2001c), clearly variable sources will be those with $I > 5$, possibly variable sources will have $2.5 < I < 5$, non-variable sources will have $I < 1.7$, and the remaining sources will be considered as dubious cases. These are very conservative cut-offs: $I > 5$ means that we are asking for the value of I to be 8σ above that of pulsars in order to classify a source as variable.

In Figure 2 we compare the I -index distribution for the samples under analysis. The mean value for AGNs (left panel) is 3.3 ± 2.6 . A possible peak in the plot is seen at $I = 2.5$, which represents a value 4σ above that presented by pulsars. An apparently extra peak appears at $I \sim 6$. Clearly, most of the AGNs are likely variable sources. The mean for the unidentified sources (Figure 2, right panel) is also high: 3.0 ± 2.3 . There are, again, apparently two distinct peaks in the distribution, located at $I \sim 2$ and $I \sim 6$.

In Figure 3 (left panel) we show the variability index I versus the Galactic latitude. The constraint we are imposing on our sample of unidentified sources (to have $|b| > 30^\circ$) can be clearly noticed in the bottom plot. There is not a clear dependence of the variability index with latitude, neither for AGNs nor for unidentified sources. The same happens in the plots of Figure 3 (right panel), where we show the variability index versus the photon spectral index. An apparent trend of increasing the variability status for the steepest sources, already noticed by Torres et al. (2001a) and Reimer (2001), is shown in this figure. However, this is not conclusive since results for a Spearman Rank test are in the range of a few percent for this to be a random phenomenon. An overall characteristic of Figures 2 and 3 is that both samples look quite similar, with no apparent strong deviation from each other shown in terms of variability or photon spectral index distributions.

Table 1. The 45 unidentified sources considered in the analysis. We list their 3EG Catalog name, their Galactic coordinates, spectral index, variability index, and the values of $\langle F \rangle$ used to define I in Eq. (2). We also provide the 3EG P1234 fluxes, F . $\langle F \rangle$ and F are in units of 10^{-8} photons $\text{cm}^{-2} \text{s}^{-1}$. The columns labeled τ , τ_{min} , and τ_{max} , give the central value of Tompkins' (1999) index for variability and their 68% CL lower and upper limit deviations, respectively. The pulsar population has $\langle \tau \rangle < 0.1$, whereas typical AGNs have $\langle \tau \rangle \sim 0.7$. Extreme upper limits for τ , whose maximum is 10000, imply possible strong variability.

3EG JSource	l	b	Spectral index	I	τ	τ_{min}	τ_{max}	$\langle F \rangle$	F
0245+1758	157.62	-37.11	2.61	2.74	2.63	0.73	2287	11.3	8.8
0404+0700	184.00	-32.15	2.65	1.50	0.34	0.00	1.65	13.5	11.1
0512-6150	271.25	-35.28	2.40	2.34	0.00	0.00	0.55	10.8	7.2
0530-3626	240.94	-31.29	2.63	1.62	17.8	15.8	0.61	0.15	2.28
0808+4844	170.46	32.48	2.15	0.90	0.00	0.00	0.39	12.2	10.7
0808+5114	167.51	32.66	2.76	1.53	0.00	0.00	0.73	13.5	8.7
0910+6556	148.30	38.56	2.20	1.79	0.49	0.00	1.14	9.2	5.9
1457-1903	339.88	34.60	2.67	2.72	0.42	0.00	3.64	13.9	8.1
1504-1537	344.04	36.38	-	2.73	10.33	1.21	9999.	12.9	8.8
1600-0351	6.30	34.81	2.65	7.26	68.17	0.00	9999.	9.7	9.9
1621+8203	115.53	31.77	2.29	0.34	0.00	0.00	0.29	11.5	7.4
1733+6017	89.12	32.94	3.00	1.82	0.39	0.00	1.38	16.9	8.7
1958-4443	354.85	-30.13	-	7.43	58.02	5.85	9999.	11.3	6.4
2034-3110	12.25	-34.64	3.43	5.26	2.88	0.89	155.	6.8	5.2
2219-7941	310.64	-35.06	2.50	1.37	0.00	0.00	0.51	19.8	13.5
2243+1509	82.69	-37.49	-	11.11	3.42	0.88	3097	7.4	9.9
2248+1745	86.00	-36.17	2.11	2.20	1.07	0.43	3.98	20.2	12.9
2255+1943	89.03	-35.43	2.36	5.54	2.31	0.80	48.6	14.2	5.8
0038-0949	112.69	-72.44	2.70	2.71	0.00	0.00	0.89	15.3	12.0
0118+0248	136.23	-59.36	2.63	2.28	5.17	0.90	9999.	11.5	5.1
0130-1758	169.71	-77.11	2.50	0.10	0.00	0.00	0.38	13.5	11.6
0159-3603	248.89	-73.04	2.89	1.26	0.00	0.00	1.16	11.9	9.8
0215+1123	153.75	-46.37	2.03	3.67	10.06	1.19	9999.	8.0	9.3
0253-0345	179.70	-52.56	-	7.99	16.44	1.38	9999.	5.0	6.2
0348-5708	269.35	-46.79	-	4.76	6.60	1.29	9999.	5.8	3.8
0917+4427	176.11	44.19	2.19	1.69	0.00	0.00	0.34	18.6	13.8
1009+4855	166.87	51.99	1.90	1.14	0.00	0.00	0.60	7.7	4.8
1052+5718	149.47	53.27	2.51	2.02	0.21	0.00	0.74	6.8	5.0
1133+0033	264.52	57.48	2.73	4.44	0.71	0.16	2.00	9.1	3.7
1134-1530	277.04	43.48	2.70	3.35	2.85	1.11	51.5	17.2	9.9
1212+2304	235.57	80.32	2.76	5.65	78.82	0.00	9999.	6.3	3.3
1219-1520	291.56	46.82	2.52	3.16	1.78	0.74	13.7	8.9	4.1
1222+2315	241.87	82.39	-	1.95	61.09	2.44	9999.	6.9	5.7
1227+4302	138.63	73.33	-	3.20	61.09	2.44	9999.	6.7	4.6
1234-1318	296.43	49.34	2.09	2.03	0.42	0.12	0.81	11.0	7.3
1235+0233	293.28	65.13	2.39	1.04	0.23	0.00	0.65	10.5	6.8
1236+0457	292.59	67.52	2.48	1.70	0.00	0.00	1.45	7.3	6.5
1310-0517	311.69	57.25	2.34	1.28	2.94	1.69	7.92	11.4	7.9
1323+2200	359.33	81.15	1.86	5.17	2.69	0.93	46.8	10.1	5.2
1337+5029	105.40	65.04	1.83	2.85	0.54	0.00	1.35	10.0	9.2
1347+2932	47.31	77.50	2.51	1.10	0.48	0.00	1.45	15.3	9.6
1424+3734	66.82	67.76	3.25	1.90	0.01	0.00	9999.	18.0	-
2241-6736	319.81	-45.02	2.39	1.25	0.00	0.00	1.09	16.6	-
2251-1341	52.48	-58.91	2.43	5.17	9.49	1.58	9999.	9.7	6.5
2255-5012	338.75	-58.12	2.79	1.59	0.41	0.00	1.46	12.7	9.2

2.3 Fluxes and possible radio counterparts

In Figure 4 we show the EGRET averaged flux as a function of the photon spectral index and the variability index, respectively. We notice that, although there is no apparent difference in the form of the distribution for both samples under consideration, there is a clear contrast on the flux values: Whereas most identified γ -ray AGNs have fluxes

above 10^{-7} photons $\text{cm}^{-2} \text{s}^{-1}$, most of the unidentified sources present lower values. This is consistent with what was presented by Gehrels et al. (2000) for sources at latitudes $|b| > 5^\circ$.

This difference in the flux values is also translated into the Log N - Log F plots we present in Figure 5. It can

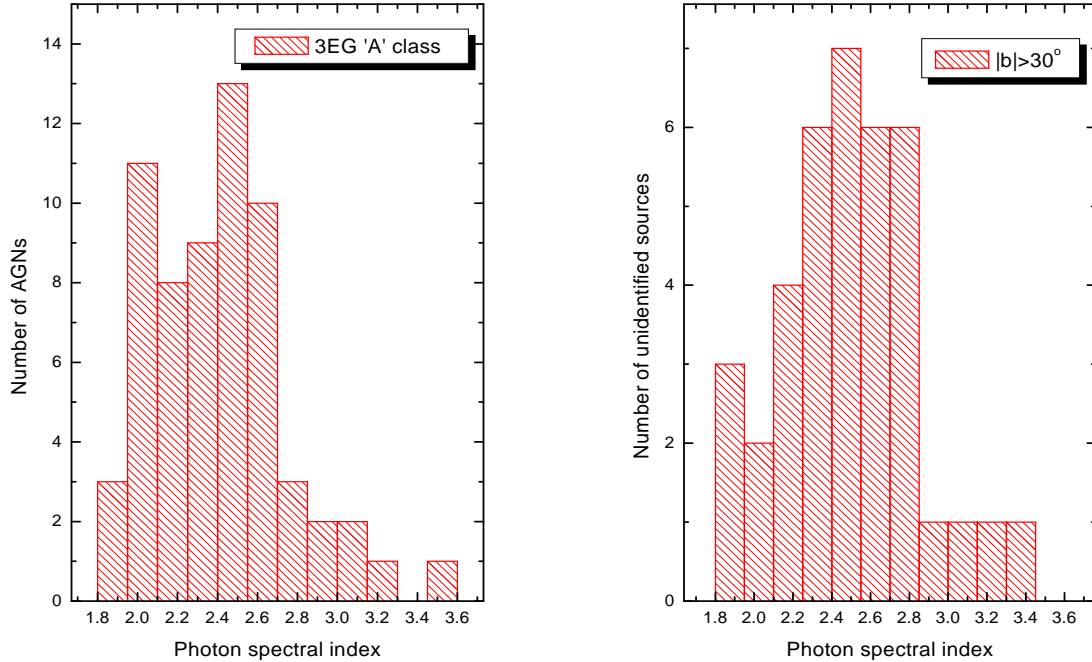


Figure 1. Photon spectral index comparison. The left panel shows the distribution for the 67 detected AGNs, dubbed A, in the Third EGRET Catalog. The right panel shows the corresponding distribution for the $|b| > 30^\circ$ unidentified sources.

be seen there that the linear fits differ significantly. AGNs present a fit close to what is expected for an isotropic and uniform population ($F^{-3/2}$), and also similar to what was found using the 2EG Catalog (Özel & Thompson 1996). The unidentified sources, however, present a steeper dependence. The difference in the flux levels is also shown in the x -axis. However, the analysis of the result for the sample of unidentified sources should be done with extra care, since the errors are far larger, as well as the number of sources considered is smaller. Additionally, AGNs present an apparent lack of sources at $F \sim 30 \times 10^{-8}$ photons $\text{cm}^{-2} \text{s}^{-1}$, which should be confirmed or falsified by future observations.

Reimer & Thompson (2001) studied in detail the $\log N - \log F$ plots obtained from 3EG sources, but including also those sources with lower confidence level (which did not appear in the published version of the 3EG catalog). They found that there is a very pronounced contrast between average and peak flux representation in a $\log N - \log F$ diagram for the sources above $|b| > 30^\circ$. This is due to the fact that sources at high latitudes are mostly detected only in some (or in many cases, only in one) viewing periods (see below), when they show their peak flux, leaving the average over the four phases of the experiment in a much lower value. The differences in fluxes between the peak

detections of both distributions, although still present, are not so strong as the ones presented in the P1234 averaged values. As we shall see below, sources showing large fluxes only in one viewing period could be particularly suitable to be explained by microlensing of gamma-ray blazars.

The differences in the $\log N - \log F$ plots can be pointing towards one of the two following possibilities:

- (i) We are looking at (at least) two different populations; for instance, AGNs and a new halo class of high-energy objects.
- (ii) These samples are formed mostly by the same kind of objects (AGNs) but they present different γ -ray flux levels. This difference could be produced as an extrinsic effect when the sources are farther away from us than those which produce the most energetic detections.

In this paper we shall explore a plausible situation in which the second possibility prevails. If behind both samples there is actually a single class of extragalactic objects, the combined $\log N - \log F$ plot should approximately follow a $N \propto F^{-3/2}$ law. The result, given in Figure 6, confirms this and it is close to the isotropic and uniform expectation (see also the comments by Reimer & Thompson 2001). This seems to be suggesting that the sample of unidentified sources under consideration is formed by many weak AGNs,

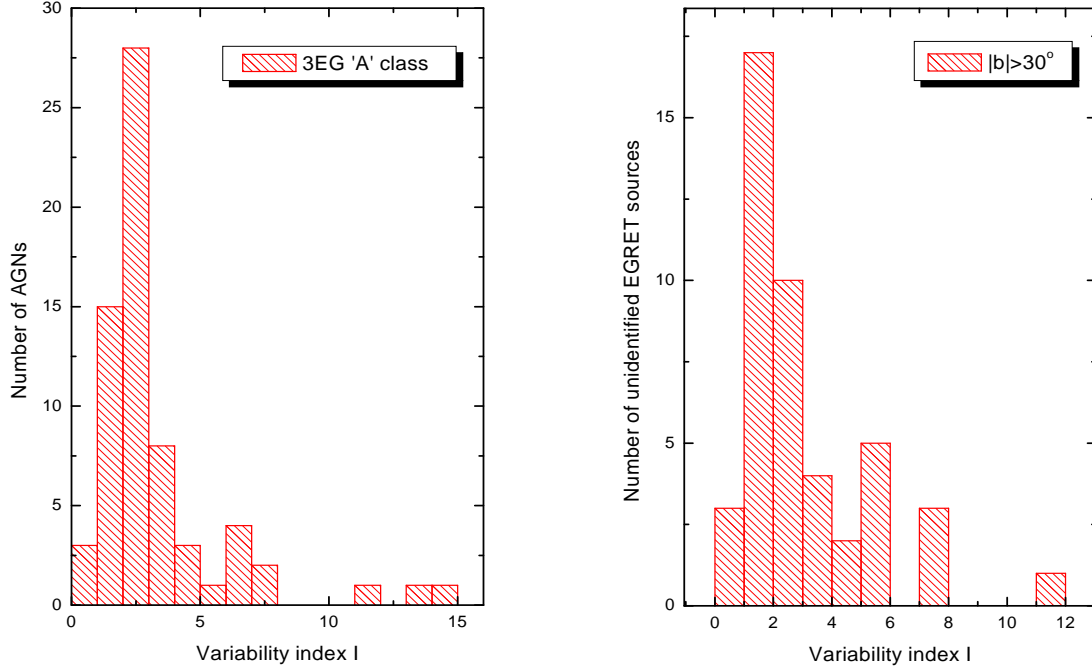


Figure 2. Variability index comparison. The left panel shows the distribution for the 67 detected AGNs, dubbed A, in the Third EGRET Catalog. The right panel shows the corresponding distribution for the $|b| > 30^\circ$ unidentified sources.

which at the same time presents a low (i.e. under the thresholds of the corresponding surveys) radio emission. We note that the apparent bump at $F \sim 30 \times 10^{-8}$ photons $\text{cm}^{-2} \text{s}^{-1}$ continues to appear in the combined plot, since no unidentified sources present such relatively high γ -ray fluxes.

Recently, Mattox et al. (2001) have presented a quantitative analysis of potential radio identifications for all 3EG sources. They used radio surveys at 5 GHz, as it was done previously for the 2EG Catalog (Mattox et al. 1997), and evaluated an a priori probability for these associations to be physical, based on the positional offsets and radio fluxes of the proposed counterparts. They found that 45 out of the 67 3EG sources classified with ‘A’ by Hartman et al. (1999) were among the EGRET identifications with the highest probability of being correct. Only one extra possible association in the list of these most likely identifications was not dubbed ‘A’ in the 3EG Catalog. For each of these 46 associations, they have compiled radio fluxes at 5 GHz, and when available, also those obtained with VLBI. In Figure 7 we show the γ -ray flux of each of these 3EG sources (note that we plot the P1234 EGRET flux of the 3EG source from Hartman et al. 1999, not the flux of the AGN quoted, for instance, in Mattox et al. 1997) as a function of the radio flux at 5 GHz of the likely counterparts. Most of the detections present a radio flux above 1 Jy, and there is an apparent trend to be-

come more radio loud when the observed γ -ray flux is higher. This is the expected behaviour when the emitted γ -rays have their origin in inverse Compton interactions of the same particle population (leptons) that generates the radio emission, targeting a soft photon field. We have superposed a linear function to the radio-gamma data that is also shown in Figure 7. There, we indicate with a dashed line, the extension of this linear fit to the region where there are no 3EG ‘A’ AGN sources. The big vertical box signals the threshold for detectability in the radio surveys used to search for counterparts (~ 30 mJy). The middle, lighter colored box, signals the range of γ -ray fluxes for the unidentified sources considered in this paper. It is apparent, then, that if weak AGNs were to approximately follow the linear fit, we could find several γ -ray sources without significant radio flux. Many of them could be those unidentified sources we are studying here. In addition, if γ -ray sources are affected by a differential gravitational lensing effect, this process, as we shall show below, would enhance only the γ -ray emission, keeping the radio fluxes at low levels. This mechanism, then, would be in agreement with what is shown in Figure 7, provided the associated sources are within the middle box on the left. Of course, this cannot apply to all unidentified sources because, otherwise, it would result in a hole in the source distribution between the already detected AGNs and the candidates, at radio flux levels of ~ 100 mJy. It should be remembered,

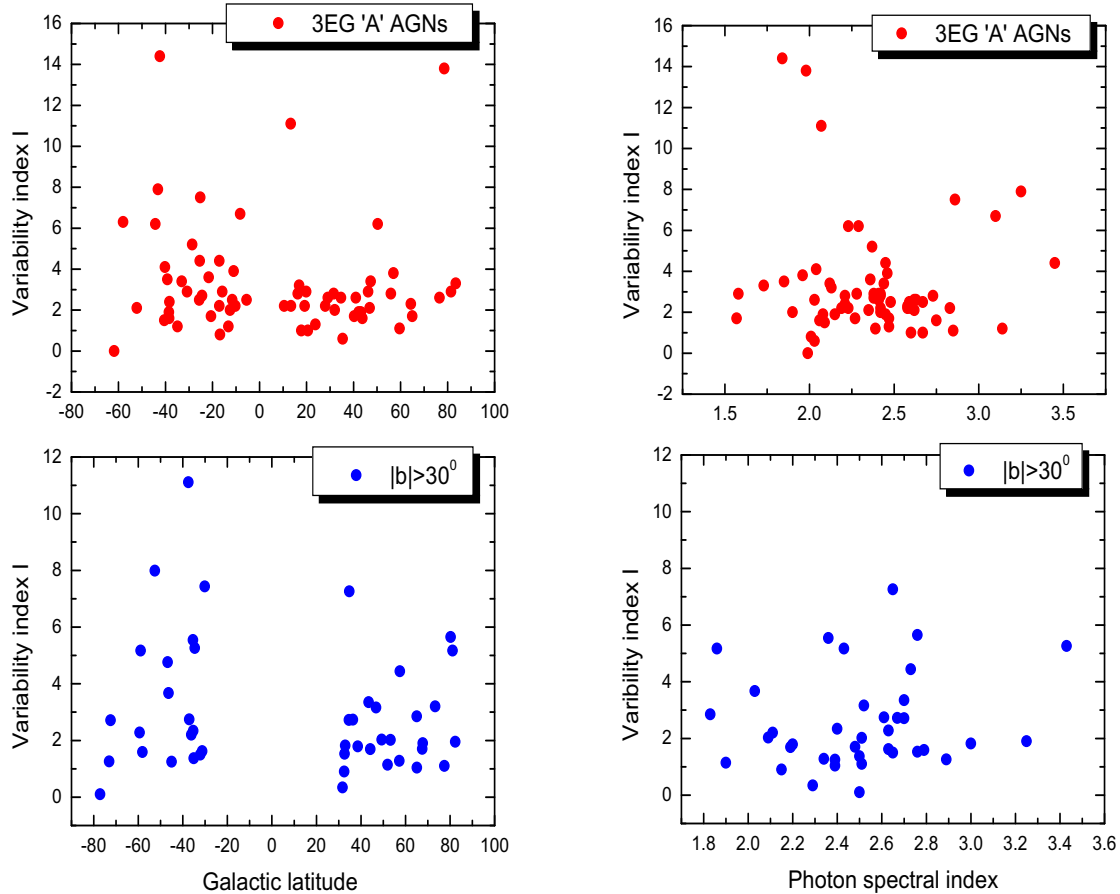


Figure 3. Variability index I (Torres et al. 2001) versus Galactic latitude (left) and versus photon spectral index (right).

anyhow, that sources at high latitude are preferentially identified by their peak flux, which can be much higher than the average. Although population studies are a powerful tool to study the nature of the unidentified detections, they should be supplemented by a source-by-source analysis.

2.4 Light curves

The most interesting candidates in order to pursue further study seem to be those sources presenting the highest levels of variability. Most AGNs are, as we have already said, variable sources, even with γ -ray emission fluctuating from detection to non-detection in successive viewing periods. We show some examples of typical light curves in Figure 8. This kind of light curves are also shown by many unidentified sources, what is consistent with the high levels of variability they present.

2.5 Assessment

To finish this section we remark our main conclusion up to here, namely, that *it is likely that some of the high-latitude unidentified sources be not more than otherwise undetected AGNs, presenting a low or nil (below any current detection threshold) radio flux.* General gamma-ray characteristics of both γ -ray blazars and high-latitude unidentified sources are very similar. There remains, however, the question of why, whereas most γ -loud blazars present radio flux at the Jy level, the unidentified sources have no strong radio counterpart at all. If the same mechanism for γ -ray production operates in both groups of objects, why are they so different at lower energies? We shall argue in the next sections that extrinsic effects can result in such a behaviour.

3 MICROLENSING

3.1 Point-like source and point-like lens

Let us consider a background and weak γ -ray emitting blazar, whose GeV flux is well below the EGRET sensitiv-

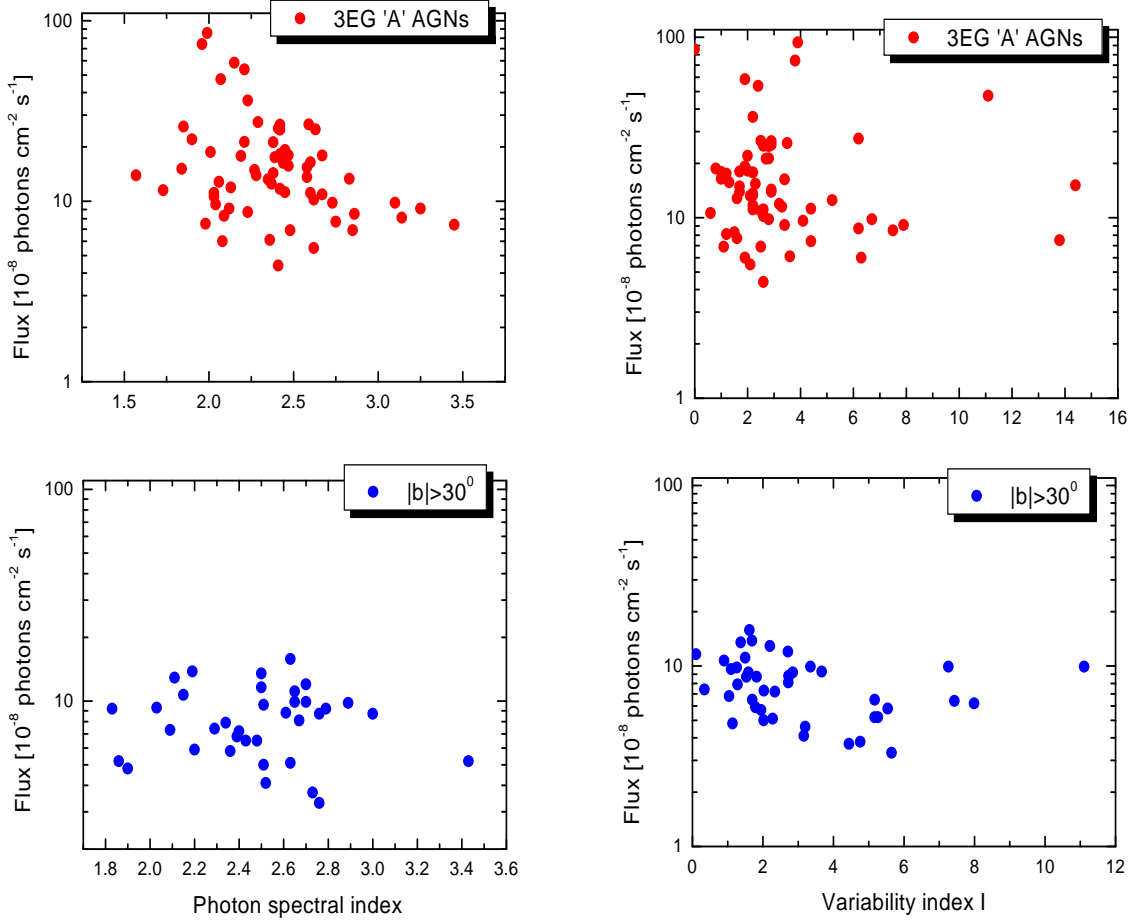


Figure 4. Source fluxes (P1234, Hartman et al. 1999) versus photon spectral index (left) and variability index (right).

ity threshold and whose radio flux is at the mJy level. We shall first use the Chang & Refsdal (1984) model. Assuming a galaxy is interposed in the line of sight, the lens equation in the lens plane for a point source is (e.g. Schneider et al. 1992):

$$\mathbf{r} - \mathbf{r}_0 - R_E^2 \frac{\mathbf{r}}{r^2} - \begin{pmatrix} \kappa + \gamma & 0 \\ 0 & \kappa - \gamma \end{pmatrix} \mathbf{r} - \mathbf{d}_0 = 0, \quad (4)$$

where the coordinate system is centered on the microlens (a star within the galaxy), with the orientation of the orthonormal basis $\{\mathbf{e}_1, \mathbf{e}_2\}$ chosen to diagonalize the quadrupole matrix; the source is at \mathbf{r}_0 and the image position is \mathbf{r} . The third term in equation (4) arises from the deflection in the lens plane due to the microlens, here considered as a point mass M . R_E is the usual Einstein radius

$$R_E = \sqrt{\frac{4GM}{c^2} \frac{D_{ol} D_{ls}}{D_{os}}}, \quad (5)$$

with D_{os} the observer-source distance, D_{ol} the observer-lens distance and D_{ls} the lens-source distance. The fourth and fifth terms in Eq. (4) arise from the deflection imprinted by

the galaxy as a whole. In the fourth term, κ and γ are the focusing and the shear of the galaxy, at the lens position, respectively. \mathbf{d}_0 depends on the deflection imprinted by the galaxy as a whole at the location of the microlens; its only effect is to change the unperturbed source position \mathbf{r}_0 by a constant. We shall ignore \mathbf{d}_0 , assuming a displaced source position $\mathbf{s} = \mathbf{r}_0 + \mathbf{d}_0$ in the lens plane.

Defining new coordinates \mathbf{X} and \mathbf{Y} , in the lens and the source plane respectively, as

$$\mathbf{X} = \frac{\sqrt{|1 - \kappa + \gamma|}}{R_E} \mathbf{r}, \quad (6)$$

and

$$\mathbf{Y} = \frac{1}{R_E \sqrt{|1 - \kappa + \gamma|}} \mathbf{s}, \quad (7)$$

the lens equation becomes

$$\mathbf{Y} = \varepsilon \begin{pmatrix} \Lambda & 0 \\ 0 & 1 \end{pmatrix} \mathbf{X} - \frac{\mathbf{X}}{|\mathbf{X}|^2}, \quad (8)$$

where

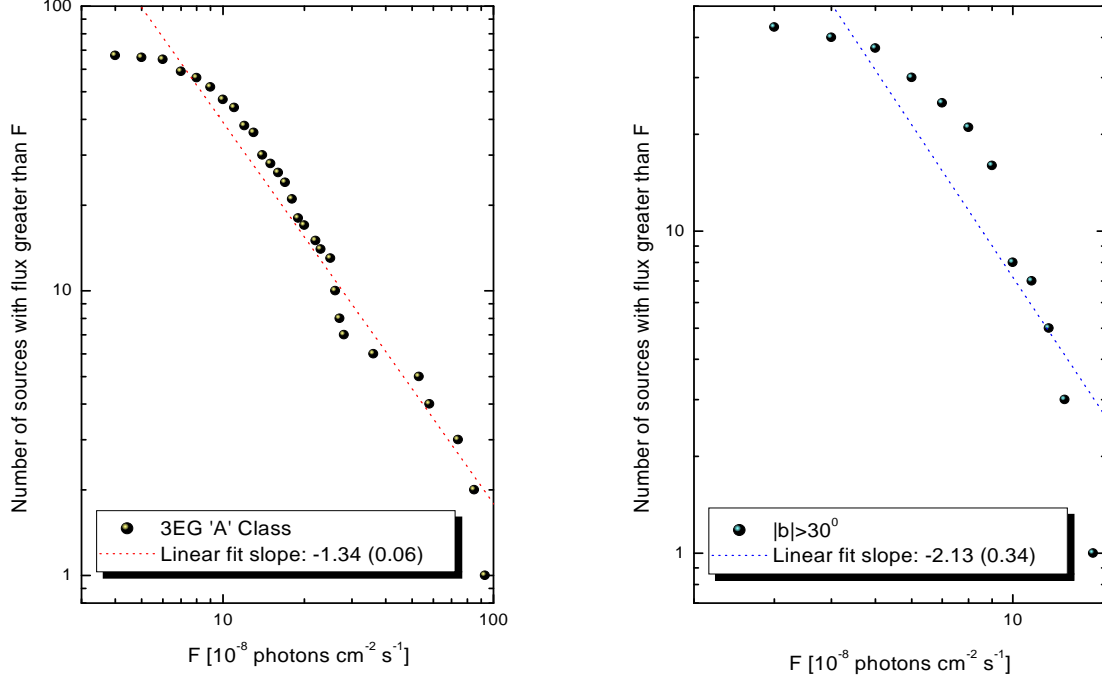


Figure 5. Log N–Log F comparison. The value of the linear fit slope (and error within parentheses) is shown for each case. F is the 3EG P1234 flux.

$$\varepsilon = \text{sign}(1 - \kappa + \gamma), \quad (9)$$

and

$$\Lambda = \frac{1 - \kappa - \gamma}{1 - \kappa + \gamma}. \quad (10)$$

The solution of equation (8) can be found reducing the problem to a fourth order equation for X^2 (Schneider et al. 1992). In order to do it we introduce new coordinates

$$X_1 = X \cos \phi, \quad (11)$$

$$X_2 = X \sin \phi, \quad (12)$$

so we obtain

$$Y_1 = \varepsilon \Lambda X_1 - \frac{X_1}{X^2} = \left(\varepsilon \Lambda - \frac{1}{X^2} \right) X \cos \phi, \quad (13)$$

and

$$Y_2 = \varepsilon X_2 - \frac{X_2}{X^2} = \left(\varepsilon - \frac{1}{X^2} \right) X \sin \phi. \quad (14)$$

Solving for $\cos \phi$ and for $\sin \phi$, we get

$$\cos \phi = \frac{Y_1}{X(\varepsilon \Lambda - 1/X^2)}, \quad (15)$$

and

$$\sin \phi = \frac{Y_2}{X(\varepsilon - 1/X^2)}. \quad (16)$$

This readily implies

$$\frac{Y_1^2}{X^2(\varepsilon \Lambda - 1/X^2)^2} + \frac{Y_2^2}{X^2(\varepsilon - 1/X^2)^2} = 1, \quad (17)$$

that translates into

$$\begin{aligned} \Lambda^2 X^8 - [2\varepsilon \Lambda (\Lambda + 1) + Y_1^2 + \Lambda^2 Y_2^2] X^6 + \\ [\Lambda^2 + 4\Lambda + 1 + 2\varepsilon (Y_1^2 + \Lambda Y_2^2)] X^4 - \\ [2\varepsilon (\Lambda + 1) + Y_1^2 + Y_2^2] X^2 + 1 = 0. \end{aligned} \quad (18)$$

Here, $X = |\mathbf{X}|$ and the sub-indices stand for the different components of the respective vectors. Equation (18) can be solved by any standard method. Since it is a fourth order equation, we can have zero, two or four real solutions to the lens equation. The number of images is then given by the number of real and positive solutions of this equation. For any real and positive solution, X^2 , we can take the positive value of X and obtain the position of the image using the definitions given in Eqs. (15–16) and (11–12) above.

The magnification $A = I_{\text{obs}}/I_0$ for any image is in turn given by the determinant of the Jacobian matrix. This can be computed using the chain rule for derivatives

$$\frac{\partial \mathbf{s}}{\partial \mathbf{Y}} \frac{\partial \mathbf{Y}}{\partial \mathbf{r}} = \frac{\partial \mathbf{s}}{\partial \mathbf{Y}} \frac{\partial \mathbf{Y}}{\partial \mathbf{X}} \frac{\partial \mathbf{X}}{\partial \mathbf{r}}, \quad (19)$$

that finally yields

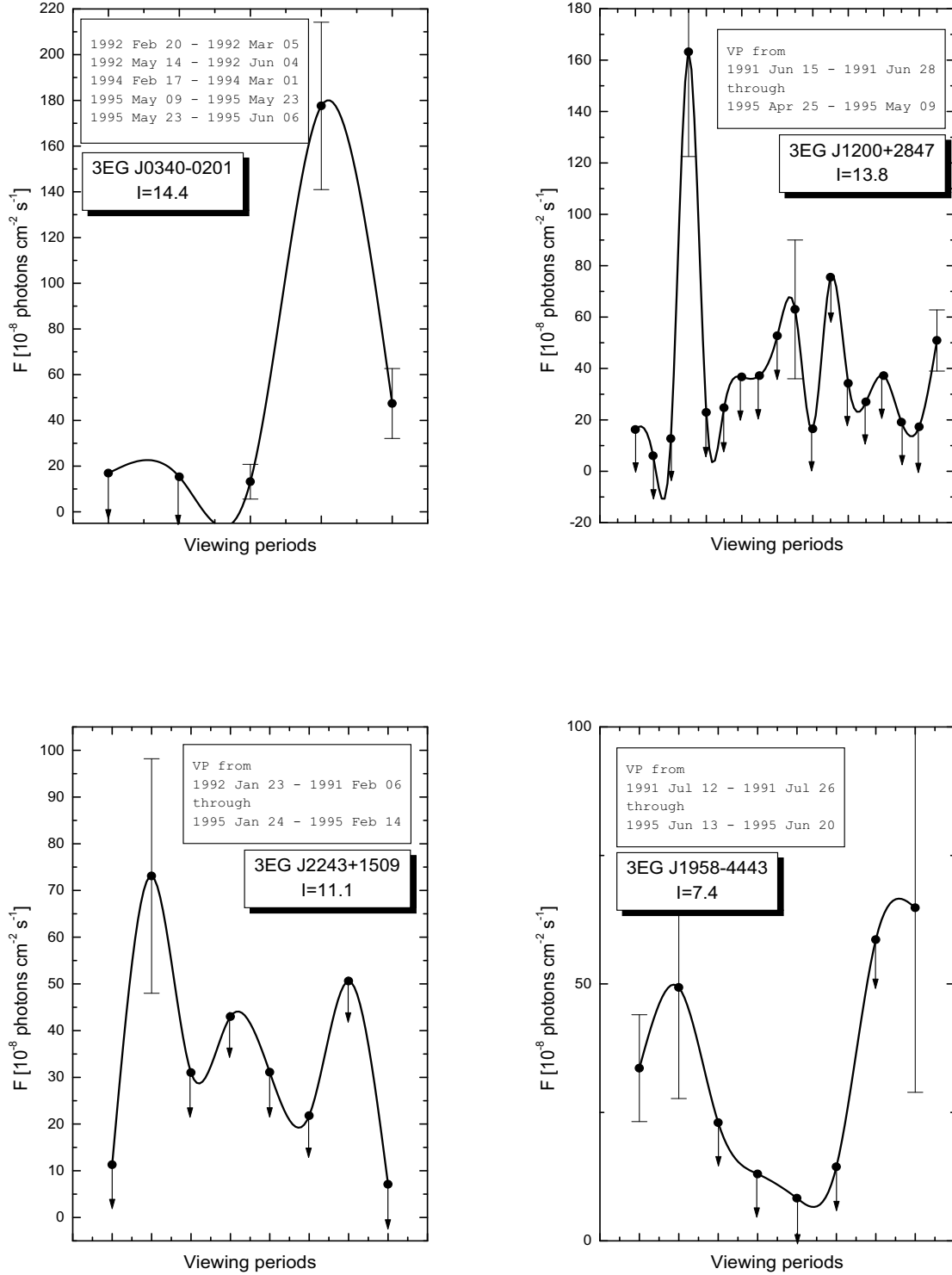


Figure 8. Examples of γ -ray light curves of 3EG ‘A’ AGNs (upper panel) and unidentified sources with $|b| > 30^\circ$ (lower panel). Cases chosen among the most variable ones are shown here. Points with arrows represent upper limits on the flux. Spline curves do not represent actual fits.

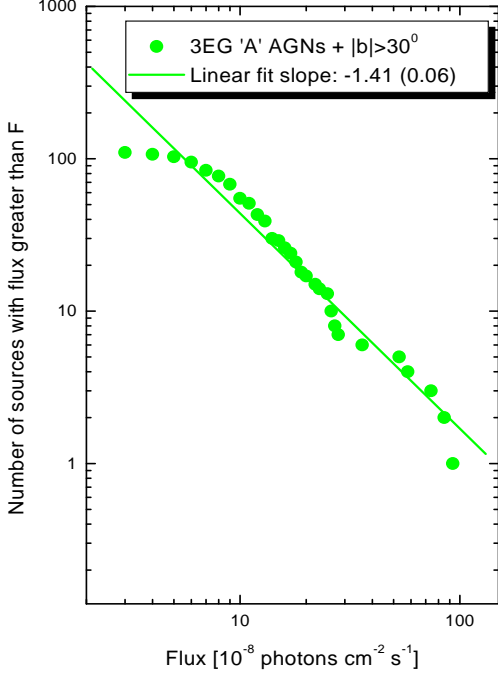


Figure 6. Log N–Log F for the combined samples. The value of the linear fit slope (and error within parentheses) is shown.

$$A = \left| \det \left(\frac{\partial \mathbf{s}}{\partial \mathbf{r}} \right) \right|^{-1} = \frac{1}{|1 - \kappa + \gamma|} \left| \det \left(\frac{\partial \mathbf{Y}}{\partial \mathbf{X}} \right) \right|^{-1}. \quad (20)$$

Since

$$\frac{\partial \mathbf{Y}}{\partial \mathbf{X}} = \begin{pmatrix} \varepsilon \Lambda + \frac{X_1^2 - X_2^2}{X^4} & \frac{2X_1 X_2}{X^4} \\ \frac{2X_1 X_2}{X^4} & \varepsilon - \frac{X_1^2 - X_2^2}{X^4} \end{pmatrix}, \quad (21)$$

then

$$A = \frac{1}{|1 - \kappa + \gamma|} \times \frac{(X_1^2 + X_2^2)^2}{\left| \Lambda (X_1^2 + X_2^2)^2 + \varepsilon (1 - \Lambda) (X_1^2 - X_2^2) - 1 \right|}. \quad (22)$$

The total magnification for a point source is

$$A_0 = \sum_{i=1}^n A_i, \quad (23)$$

where n is the number of images and A_i are obtained replacing the solutions of Eq. (8) in Eq. (22).

The curves for which the determinant of the Jacobian matrix is zero are called critical curves. For the Chang-Resfdal lens, these critical curves are Cassini ovals given by the equation

$$\Lambda (X_1^2 + X_2^2)^2 + \varepsilon (1 - \Lambda) (X_1^2 - X_2^2) - 1 = 0. \quad (24)$$

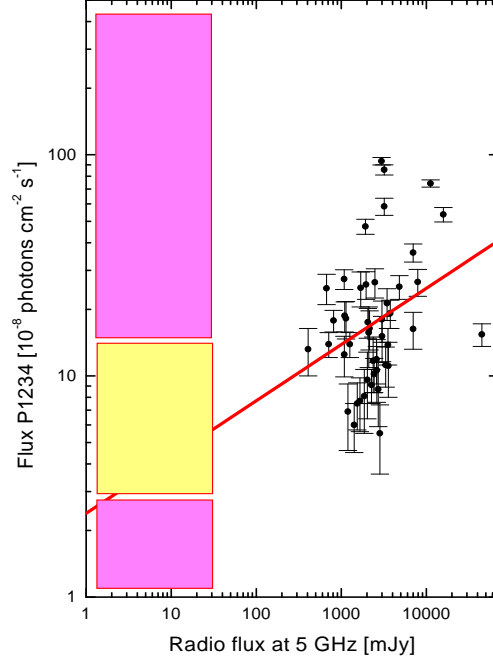


Figure 7. Radio and γ -ray fluxes of the 46 most likely AGN detections. The big vertical box signals the threshold sensibility in the radio surveys used to search for counterparts (~ 30 mJy). The middle box signals the range of γ -ray fluxes for the unidentified sources considered in these paper.

The caustics are the mappings of the critical curves, through the lens equation, onto the source plane. When the source crosses a caustic, the number of images changes by two, and, if a point source is on a caustic, the magnification diverges. In realistic situations, sources are extended instead of point-like, and when the source is on (or near) a caustic the magnification is finite (although large).

When $\gamma = 0$ (no shear case), $\Lambda = 1$, and the lens geometry becomes axially symmetric (notice also that the caustic curve collapses to a point). Then, we can use the one-dimensional lens equation:

$$Y = \varepsilon X - \frac{1}{X}, \quad (25)$$

which has as solutions

$$X_{\pm} = \frac{\varepsilon Y}{2} \pm \sqrt{\frac{Y^2}{4} + \varepsilon} \quad (26)$$

for $Y^2 > -4\varepsilon$. Hence, for $\varepsilon = 1$ we always have two solutions, and when $\varepsilon = -1$ there are two solutions for $|Y| > 2$ and none for $|Y| < 2$. The magnification of any image is

$$A_{\pm} = \frac{1}{|1 - \kappa|} \frac{X_{\pm}^4}{|X_{\pm}^4 - 1|}, \quad (27)$$

and the total magnification is given by

$$A_0 = A_+ + A_-. \quad (28)$$

Replacing Eq. (27) in Eq. (28) and using Eq. (26), we arrive at

$$A_0 = \frac{1}{|1 - \kappa|} \frac{Y^2 + 2\varepsilon}{|Y| \sqrt{Y^2 + 4\varepsilon}}. \quad (29)$$

Some tricky –although straightforward– algebra used to arrive at the previous equation is described in the Appendix. In this case, we have the critical curve at $X = 1$, which gives a degenerate caustic at $Y = 0$ for $\varepsilon = 1$, and a circular caustic of radius $Y = 2$ for $\varepsilon = -1$.

3.2 Extended source

For an extended circular source, the light curve is given by (see e.g. Han et al. 2000):

$$A = \frac{\int_0^{2\pi} \int_0^{r_s} \mathcal{I}(r, \varphi) A_0(r, \varphi) r dr d\varphi}{\int_0^{2\pi} \int_0^{r_s} \mathcal{I}(r, \varphi) r dr d\varphi}, \quad (30)$$

where (r, φ) are polar coordinates in a reference frame placed in the center of the source, r_s is the radius of the source and $\mathcal{I}(r, \varphi)$ is the surface intensity distribution of the source. For a uniform distribution this produces a simplified expression,

$$A = \frac{\int_0^{2\pi} \int_0^{r_s} A_0(r, \varphi) r dr d\varphi}{\pi r_s^2}. \quad (31)$$

Introducing the dimensionless radial coordinate $R = r/R_E$, we obtain

$$A = \frac{\int_0^{2\pi} \int_0^{R_s} A_0(R, \varphi) R dR d\varphi}{\pi R_s^2}, \quad (32)$$

where $R_s = r_s/R_E$ is the corresponding dimensionless radius of the source.

We assume that the microlens is moving with constant velocity \mathbf{v} and we choose the origin of time ($t = 0$) as the instant of closest approach between the lens and the source. Then, if the center of the source is placed at $t = 0$ in $\mathbf{b} = (b_1, b_2)$, the position of any point of the source with polar coordinates (r, φ) is:

$$s_1(t) = b_1 - vt \cos \theta + r \cos \varphi, \quad (33)$$

$$s_2(t) = b_2 - vt \sin \theta + r \sin \varphi, \quad (34)$$

where $v = |\mathbf{v}|$, θ is the angle between \mathbf{v} and \mathbf{e}_1 , $0 < r < r_s$ and $0 < \varphi < 2\pi$. Figure 9 shows these geometrical considerations.

Plugging Eqs. (33-34) into Eq. (7), we obtain

$$Y_1 = \frac{b_1 - vt \cos \theta + r \cos \varphi}{R_E \sqrt{|1 - \kappa + \gamma|}}, \quad (35)$$

$$Y_2 = \frac{b_2 - vt \sin \theta + r \sin \varphi}{R_E \sqrt{|1 - \kappa + \gamma|}}. \quad (36)$$

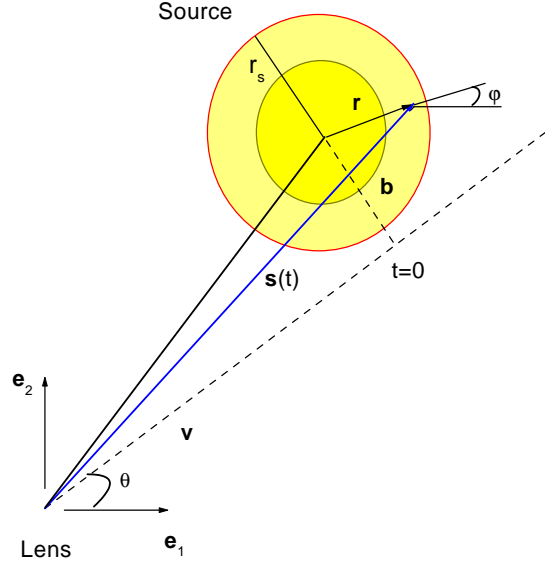


Figure 9. Geometrical sketch of an extended source and physical variables. All points of the source must be taken into account when computing the magnification in a microlensing event.

In units of the Einstein radius, these equations transform into

$$Y_1 = \frac{B_1 - T \cos \theta + R \cos \varphi}{\sqrt{|1 - \kappa + \gamma|}}, \quad (37)$$

$$Y_2 = \frac{B_2 - T \sin \theta + R \sin \varphi}{\sqrt{|1 - \kappa + \gamma|}}, \quad (38)$$

where $T = vt/R_E$, $B_1 = b_1/R_E$ and $B_2 = b_2/R_E$. When $\gamma = 0$ (no shear), we can take $\theta = 0$ and $\mathbf{B} = (0, B_0)$ in the above expressions without losing generality.

4 γ -RAY BLAZARS AS SOURCES

The fact that some γ -ray blazars have been observed to flare dramatically on time scales of days imposes severe constraints on the size of the emitting region. The optical depth for intrinsic $\gamma + \gamma \rightarrow e^+ + e^-$ attenuation is (e.g. Schlickeiser 1996):

$$\tau \simeq \sigma_T n_\gamma R = \frac{\sigma_T}{4\pi c \langle \epsilon \rangle} l, \quad (39)$$

where σ_T is the Thompson cross section, n_γ the γ -ray photon density, $R < ct_v$ the source size inferred from the intrinsic variability time scale, $\langle \epsilon \rangle$ the mean photon energy, and l the compactness parameter defined as the ratio of the intrinsic source luminosity to its radius. The optical depth can be written as:

$$\tau > 200 \frac{L_{48}}{t_v/1 \text{ day}}, \quad (40)$$

with L_{48} the luminosity in units of 10^{48} erg s $^{-1}$. For typical values $t_v \sim 1$ day and $L_{48} \sim 1$, the source is opaque, contrary to the observed fact that γ -ray blazars present a power-law γ -ray spectrum over several decades of energy. This rules out isotropic emission in the rest frame. The emission, consequently, should be beamed. It is usually thought to be produced in a relativistic jet through inverse Compton scattering of lower energy photons (e.g. Blandford & Levinson 1995). The soft, seed photons for the Inverse Compton process could originate as synchrotron emission from within the jet, or they could come from the accretion disk surrounding the central supermassive compact object, or they could be disk radiation reprocessed in the broad line region. In the last two cases the seed photons are external to the jet itself.

In addition to these leptonic models, some hadronic alternatives have been proposed in the literature. The γ -ray emission would be produced in this case by relativistic protons interacting with ambient matter, radiation fields, or the magnetic field of the jet. For reviews and references the reader can see von Montigny et al. (1995) and Mukherjee (2001).

Independently of how the γ -rays are produced, they must traverse the strong X-ray field produced in the innermost region of the accretion disk. The observed γ -ray photons cannot originate from a too small radius, otherwise they will be absorbed through pair creation in the disk photosphere (e.g. Becker & Kafatos 1995, Blandford & Levinson 1995). This naturally leads to the concept of γ -spheres in AGNs: for each γ -ray photon energy there is a radius r_γ beyond which the pair production opacity to infinity equals unity (Blandford & Levinson 1995). The size of the γ -sphere will depend on both the energy of the γ -ray photons and the soft photon flux.

For an isotropic, power-law, central source of soft photons scattered by free electrons in a warped disk, Blandford & Levinson (1995) obtain:

$$r_\gamma(E) \propto E^p, \quad (41)$$

with p depending on the details of the central source. A similar result is obtained for pure disk emission (Becker & Kafatos 1995, Romero et al. 2000). Typically, $p \in [1, 2]$. The larger γ -spheres, then, are those for the higher photon energies. This energy-dependency of the source size will naturally lead to chromaticity effects during microlensing events.

5 LIGHT CURVES AND SPECTRA OF SINGLE POINT LENSES EMBEDDED IN SMOOTHLY DISTRIBUTED MATTER

Now we focus our study on the lensing of an extragalactic γ -ray source. For immediate use, we shall define a reference source having a radius r_{ref} and a γ -ray energy E_{ref} such that

$$R_\gamma(E) = R_{\text{ref}} \left(\frac{E}{E_{\text{ref}}} \right)^p, \quad (42)$$

where $R_\gamma(E) = r_\gamma(E)/R_E$ and $R_{\text{ref}} = r_{\text{ref}}/R_E$.

We shall assume that the intensity of the source (without yet being lensed) is uniform, and that its spectrum approximately follows a power law

$$I_0(E) \propto E^{-\xi}, \quad (43)$$

with $\xi \in (1.7, 2.7)$ (Krolik, 1999). Then

$$I_0(E) = I_{\text{ref}} \left(\frac{E}{E_{\text{ref}}} \right)^{-\xi}, \quad (44)$$

where I_{ref} is the intensity of the reference source. The surface intensity distribution of the source finally ends being

$$\mathcal{I}_0(E) = \frac{I_0(E)}{\pi (R_\gamma(E))^2}. \quad (45)$$

Since $\mathcal{I}_0(E)$ does not depend on (R, φ) we can write

$$A = \frac{\int_0^{2\pi} \int_0^{R_\gamma(E)} A_0(R, \varphi) R dR d\varphi}{\pi (R_\gamma(E))^2}. \quad (46)$$

Using that $A = I/I_0$ and Eq. (44), we have

$$I = AI_0 = AI_{\text{ref}} \left(\frac{E}{E_{\text{ref}}} \right)^{-\xi}. \quad (47)$$

We define, for plotting purposes, the ratio

$$J \equiv \frac{I}{I_{\text{ref}}} = A \left(\frac{E}{E_{\text{ref}}} \right)^{-\xi}, \quad (48)$$

as the intensity in units of I_{ref} . We shall as well define the dimensionless impact parameter $u = B/R_\gamma$, with $B = \sqrt{B_1^2 + B_2^2}$. Throughout the rest of this paper we shall adopt $p = 1.1$, $\xi = 2$, and a reference source with dimensionless radius $R_{\text{ref}} = 2 \times 10^{-3}$ at a γ -ray energy of $E_{\text{ref}} = 0.1$ GeV. Results are, however, of a generic nature, and remain self-similar under reasonable variations of these parameters.

5.1 Galactic model

We shall now assume a parameterization for the mass distribution in the interposed galaxy. This will allow us to compute the values of κ_s and γ . In this Section, we assume for illustrative purposes that all matter in the lensing galaxy is smoothly distributed except for a single point lens. The full non-linear treatment for large number of lenses will be done in Section 7. If the center of the galaxy is located at $\mathbf{x}_c = (b, 0)$ in the lens plane, and if its total mass is described by a surface density Σ given by

$$\Sigma = \frac{\Sigma_c a_g}{\sqrt{a_g^2 + (x-d)^2 + y^2}}, \quad (49)$$

where Σ_c is the density at the center of the galaxy, a_g is the core radius of the galaxy, and d is the distance of the microlens to the center of the galaxy, then the focusing and shear can be written as (Schneider et al. 1992, Romero et al. 1995):

$$\kappa_s = \frac{\Sigma_c}{\Sigma_{\text{crit}}} \frac{a_g}{\sqrt{a_g^2 + d^2}}, \quad (50)$$

$$\gamma = \frac{\Sigma_c}{\Sigma_{\text{crit}}} \left(\frac{a_g}{\sqrt{a_g^2 + d^2}} - \frac{2a_g \sqrt{a_g^2 + d^2}}{d^2} + \frac{2a_g^2}{d^2} \right), \quad (51)$$

where Σ_{crit} is the critical density, defined by

$$\Sigma_{\text{crit}} \equiv \frac{c^2 D_s}{4\pi G D_l D_{ls}}. \quad (52)$$

Defining $m = \Sigma_c / \Sigma_{\text{crit}}$ and $\chi = d/a_g$, we have

$$\kappa_s = m \frac{1}{\sqrt{1 + \chi^2}}, \quad (53)$$

$$\gamma = m \left(\frac{1}{\sqrt{1 + \chi^2}} - \frac{2\sqrt{1 + \chi^2}}{\chi^2} + \frac{2}{\chi^2} \right). \quad (54)$$

When $\chi \ll 1$, γ adopts a simpler expression,

$$\gamma = m \frac{\chi^2}{4} \left(\frac{3}{2}\chi^2 - 1 \right). \quad (55)$$

If the microlens is placed at a distance from the center of the galaxy far smaller than the core radius, $d \ll a_g$, then $\chi \approx 0$ and the lensing parameters result in $\gamma = 0$, $\kappa_s = m$. We shall then adopt $\gamma = 0$, $\kappa_s = 0.8$, in the zero shear case, as an example. To study other situations, where γ can not be neglected, we shall take, $m = 2$, $\chi = 10 \Rightarrow \kappa_s = 0.20$, $\gamma = -0.16$.

5.2 Model results and analysis for a single point lens

Results for the first group of parameters (shear equal to zero) are plotted in Figure 10, for different impact distances. It can be seen there that *background AGN γ -ray emission above 100 MeV can be magnified by a very large factor in single events*. This magnification can make an otherwise unnoticed background source to exceed the detection threshold, and to be detected only when lensed. Note also the chromaticity effect: *the γ -sphere corresponding to 10 GeV, whose size is similar to the radio emitting regions of AGNs, is negligibly magnified, while the lower energy curves -but still with energies in the EGRET range, 100-500 MeV- all show significant magnifications* This phenomenon also has a spectral signature, produced by the differential magnification of the different γ -spheres (see the discussion below). The magnification grows with the focusing. The same happens, as expected, when the impact parameter is smaller.

A critical requirement for such a microlensing event to occur is that the size of the background source projected onto the lens plane is not larger than the Einstein ring of the lensing mass. Only background sources whose size is a fraction of the Einstein radius will then be significantly magnified. Since AGNs have emission regions of different scales for different radiation wavelengths, we expect a differential magnification, as observed in Figure 10. The most internal regions of AGNs, responsible for the γ -ray emission, have sizes about 10^{14} – 10^{15} cm (Blandford & Levinson 1995). Then, they can be significantly magnified. At the same time, since radio emission is originated far

down the jet, the sizes of its emitting region ($> 10^{17}$ cm) exceeds the Einstein radius of the lenses and lead to the absence of counterparts at lower frequencies.

In Figure 11, we present a completely different behavior produced when the lensing parameter γ , the shear, is different from zero. We show the results for $\kappa_s = 0.20$, $\gamma = -0.16$, and $\theta = 0^\circ$. θ (see Figure 9), is just the angle between the direction of the lens movement and the \mathbf{e}_1 unit vector, in the source plane.

In the cases of Figure 11, for the less energetic γ -spheres with energies in the range 0.1–1 GeV, there appears two (instead of one) enhancements of intensity, and with a very peculiar time profile. In the case of impact parameter $u = 0.5$, the intensity first rise relatively slowly compared with the immediately subsequent behavior, and suddenly decreases. Afterwards, this effect repeats itself in a specular way. This phenomenon is reminiscent of that found for putative matter violating some of the energy conditions (e.g. Safonova et al. 2001, Eiroa et al. 2001), although in that case, a non-zero shear is not needed in order to produce it and the flux rising is sharper.

In Figure 12, we show the size and shape of the caustics (in the source plane) for two specific lens-source configurations and lensing parameters. We also present, for comparison, the sizes of the γ -spheres for different energies. It is possible to see, then, that the biggest γ -sphere here considered, the one corresponding to $E = 10$ GeV, is larger even than the caustic size for the lensing parameters used in the left panel of the Figure. It is for this γ -sphere that we see only one intensity enhancement, translated into a peak of the magnification. The reason is that light from different parts of the source smooth down the enhancement produced by the only part crossing the caustic. Therefore, for the biggest γ -ray sphere, the caustic curve is seen as a point. However, for the smaller γ -spheres, the relative motion of the lens and source makes the latter to encounter two caustics, leading to different peaks in the time profile. Contrary to the caustic presented in the left panel of Figure 12, the lensing parameters used for the right panel produce a caustic curve actually formed by two separated pieces. When $\theta = 0$ there would not be a direct crossing of the caustic, even for the largest γ -spheres. Two peaks profiles would be explained by double caustic crossing. In this case, we would see two peaks even for the largest γ -spheres.

5.3 Spectral evolution

The differential magnification makes its way to a spectral slope change at medium energies (see Figures 10 and 11, right panels). This break, that we predict as a distinctive feature for microlensing events of γ -ray blazars, together with its peculiar time evolution –it is shifted towards high energies as times goes by since transit– can be used to differentiate this from other phenomena. The temporal evolution of the break for the cases of zero shear is shown in Figure 13.

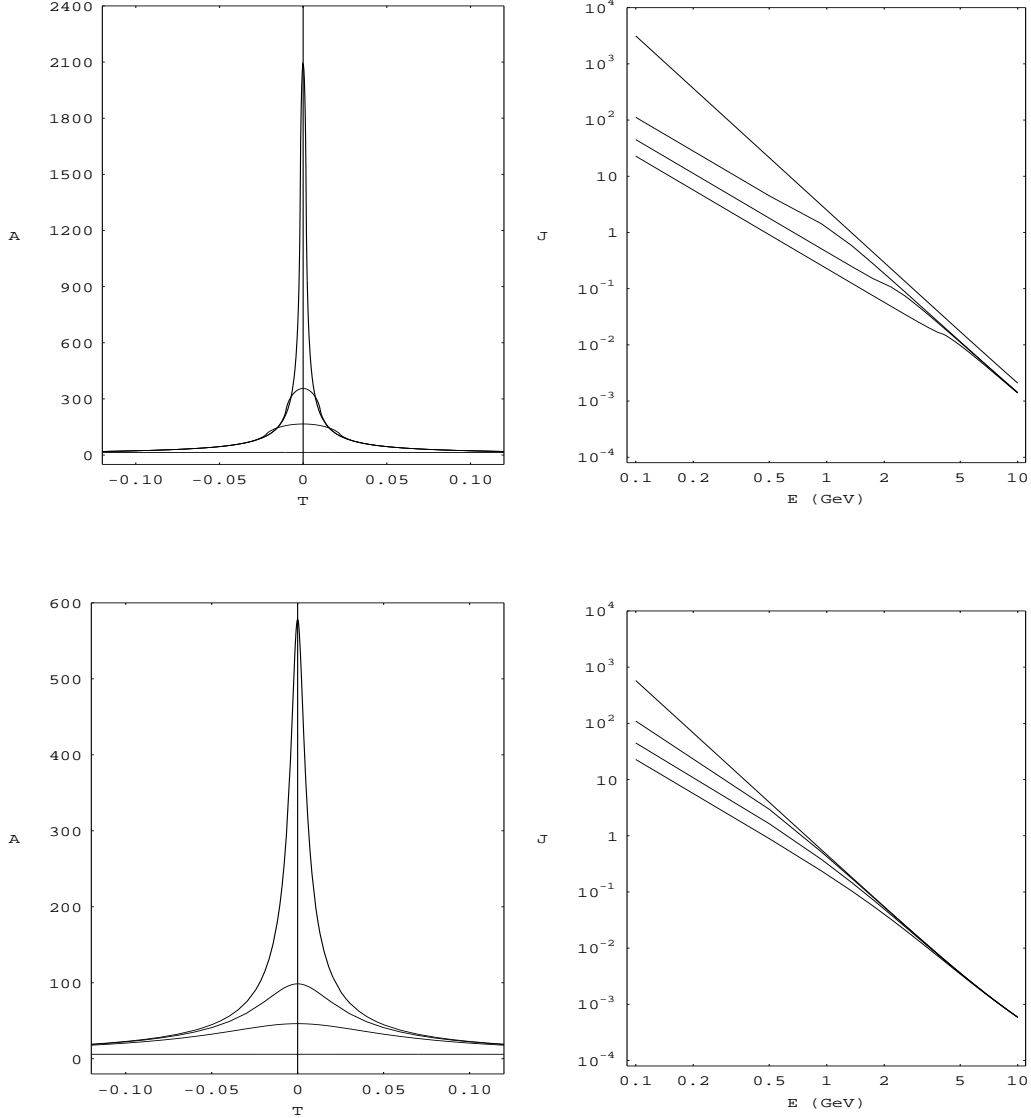


Figure 10. Lensing results for a single point lens with an impact parameter $u = b/r_s = B/R_s = 0.5$ (upper panel) and 2 (lower panel). Left: light curves, from top to bottom $E = 0.1$ GeV, 0.5 GeV, 1 GeV, 10 GeV. Right: spectra, from top to bottom $T = vt/R_E = 0, 0.02, 0.05$ and 0.10. Lensing parameters were chosen as $\kappa_s = 0.8$ and $\gamma = 0$.

The spectral evolution shown by lensing with non-zero shear is notoriously modified. In Figure 11, for instance, the spectral evolution starts at $T = 0$, then the intensity grows towards higher energies because of the encounter of the right peak in the left hand side of the left panel plots, and then continues downward as the lens gets away from the caustic. As it can be seen in Figure 11 and successive ones, it is not possible to plot in this case the evolution of the spectral break with time as a continuous function. The break in the spectrum appears only once in this energy range, for the earliest time, and then presumably moves upwards, to energies corresponding to non-magnified γ -spheres. The evolution of

the spectrum itself (and not of the position of the break) is what can help to decide in these cases if the putative observations are associated to a microlensing event.

6 OPTICAL DEPTH

6.1 Time scale

The characteristic time of a microlensing event is the time that the source takes to cross the Einstein radius of the lens. It is given by

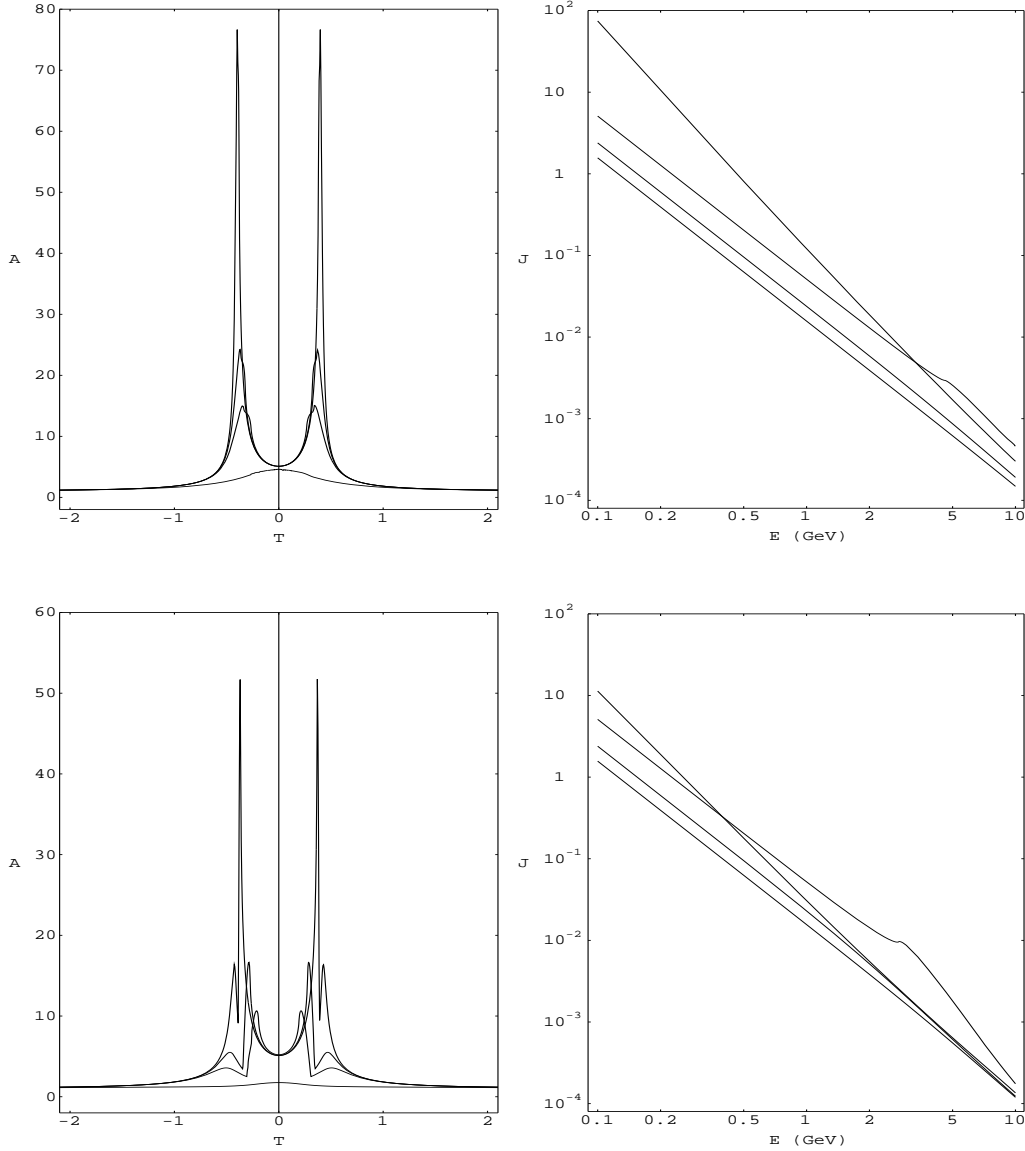


Figure 11. Lensing results for a single point lens with an impact parameter $u = 0.5$ (upper panel) and 2 (lower panel). Left: light curves, from top to bottom $E = 0.1$ GeV, 0.5 GeV, 1 GeV, 10 GeV. Right: spectra, from top to bottom $T = vt/R_E = 0.4, 0, 0.8$ and 1.2. Lensing parameters were chosen as $\kappa_s = 0.20$ and $\gamma = -0.16$ and $\theta = 0^0$.

$$t_0 = \frac{R_E}{v} = \left(\sqrt{\frac{4GM}{c^2} \frac{D_{ol} D_{ls}}{D_{os}}} \right) v^{-1}, \quad (56)$$

where v is the lens velocity. For a cosmological source, using the Friedmann-Lemaître-Robertson-Walker model of the universe, with z the redshift of the object, and the Hubble parameter H_0 and the current ratio between the actual and the critical density of the universe Ω_0 being well constrained in the range

$$50 \frac{\text{km}}{\text{s Mpc}} < H_0 < 100 \frac{\text{km}}{\text{s Mpc}}, \quad (57)$$

$$0.1 < \Omega_0 < 1, \quad (58)$$

we have

$$D(z_i, z_j) = \frac{2c}{H_0} \frac{(1 - \Omega_0 - G_i G_j)(G_i - G_j)}{\Omega_0^2 (1 + z_i)(1 + z_j)^2}, \quad (59)$$

with

$$G_{i,j} = (1 + \Omega_0 z_{i,j})^2. \quad (60)$$

Taking as an example, $H_0 = 75 \text{ km s}^{-1} \text{ Mpc}^{-1}$, $\Omega_0 = 0.2$, a lens mass of $M = 0.1 M_\odot$, a velocity $v = 5000 \text{ km s}^{-1}$, $z = 0.1$ for the lens, and $z = 1$ for the source, we obtain

$$t_0 = 1.5 \times 10^7 \text{ s} \simeq 170 \text{ days} \quad (61)$$

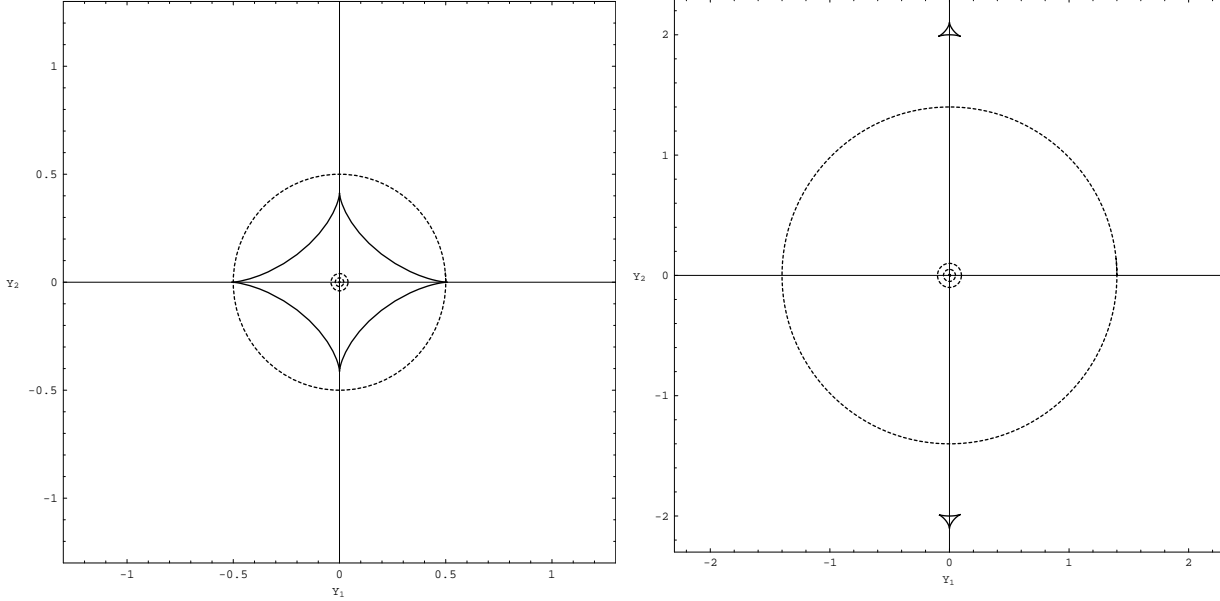


Figure 12. Left: Caustics for $\kappa_s = 0.20$ and $\gamma = -0.16$ (diamond shaped curve). Right: Caustics for $\kappa_s = 0.89$ and $\gamma = -0.34$ (triangle shaped curves). Sources inside the caustic have four images and those outside have two. The dashed circles are the gamma spheres, the bigger one corresponding to $E = 10$ GeV, then, 1, 0.5, and 0.1 GeV.

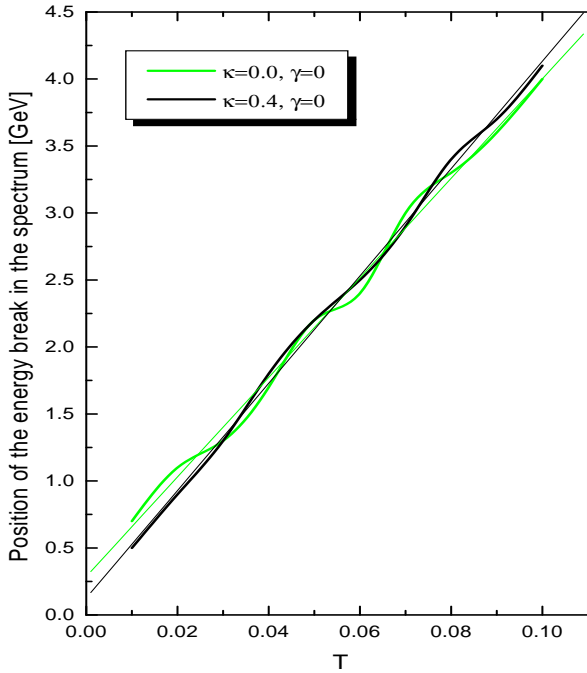


Figure 13. Temporal evolution of the spectral break in models with zero shear. The thinner solid lines represent linear fits, showing the general trend to increase the energy at which the spectral break is produced as a function of time. The impact parameter in this example is $u = 0.5$. The x-axis is $T = vt/R_E$.

The width of the peaks in the light curves (see Figure 10) is about

$$\Delta t \simeq 0.05t_0 \simeq 7.5 \times 10^5 \text{ s} \simeq 9 \text{ days}. \quad (62)$$

These numbers would change to 1202 days and 60 days, respectively, if the lensing were produced by a $5M_\odot$ star. It is interesting to compare such numbers with typical timescales of high-latitude sources determined through the EGRET experiment. The Third EGRET catalog was constructed during a period of six years, dividing the total time span in viewing periods with a duration of about 15 days. Then, when the mass of the lensing object is sub-solar, each peak in a microlensing light curve can be completely within a single EGRET viewing period: the phenomenon can lead, in principle, to a very variable source, with γ -ray fluxes varying from detection to upper limits in consecutive viewing periods. On the contrary, for a $5M_\odot$ star, a single peak would last several viewing periods and the γ -ray source could appear as a steady, non-variable detection.

6.2 Linear size of the source

We have mentioned before that in order for a microlensing event to occur, the linear size of the source, x , should be less than the Einstein radius,

$$x < 2R_E \frac{D_{os}}{D_{ol}}. \quad (63)$$

For the same typical redshifts considered in the previous section

$$R_E = 2.23 \times 10^{16} \left(\frac{M}{M_\odot} \right)^{1/2} \text{ cm}, \quad (64)$$

and we can then obtain the following relationship between the source size and the mass of the lens:

$$x < 6.37 \times 10^{17} \left(\frac{M}{M_{\odot}} \right)^{1/2} \text{ cm.} \quad (65)$$

For a source with $x = 10^{14}$ cm strong magnification occurs for stars with masses $M/M_{\odot} \geq 2 \times 10^{-3}$. This makes most of the stars MACHO-like objects in a galaxy able to produce strong gravitational lensing effects upon the innermost regions of background active galactic nuclei. The smaller masses can give rise to very rapid events (Romero et al. 1995).

6.3 Expected number of microlensing cases in γ -ray catalogs

The concept of optical depth, Γ , was originally introduced in gravitational microlensing studies by Ostriker and Vietri (1983), and it was later applied by Paczyński (1986). If Γ is smaller than unity, it provides a measure of the probability of microlensing. Alternatively, Γ can be defined as the ratio of the surface mass density of microlensing matter to the critical mass density of the galaxy (Paczynski 1986). The value of Γ depends on the model adopted for the matter distribution along the line of sight.

It is usually assumed that the a priori probability of finding a small group of distant, gravitationally magnified objects is below 1%. Recent results (Wyithe & Turner 2002), taking into account the clustering of stars in interposed galaxies, give for the a priori probability of finding magnified sources in random directions of the sky values between $10^{-2} - 10^{-3}$. In those directions where there is gravitational lensing, the probability of having large local values of optical depth is high.

The high surface mass density associated with the core of normal galaxies along with the usual assumption that most of this mass is under the form of compact objects naturally leads to high optical depths for microlensing. For instance, in the case of the lensed quasar Q2237+0305, where four images are well-resolved, lensing models indicate values of $\tau \sim 0.5$ (Schneider et al 1988; Wambsganss & Paczyński 1994), which are corroborated by the detections of microlensing-based optical variability with relatively high duty cycles (e.g. Corrigan et al. 1991, Wozniak et al. 2000, Witt & Mao 1994). Other lensed sources display even higher duty cycles (e.g. Koopmans & de Bruyn 2000).

In our case, the number of potential compact γ -ray emitting background sources is large. The last version of the Véron-Cetty & Véron's (2001) Catalog –which is still very incomplete at high redshifts– contains more than 10^3 already identified blazars, in addition to more than 10^4 quasars and other less energetic AGNs. The GLAST mission itself is expected to pinpoint about 10^4 γ -ray emitting blazars with unparalleled resolution (Gehrels & Michelson 1999); also the number of unidentified sources at high latitudes is expected to be large. If the actual total

number of γ -ray emitting blazars is in excess of, say, 10^7 , (1 blazar out of 10 000 normal galaxies) they could produce many of the expected detections by GLAST. Even when considering reduced probabilities for microlensing, scaling as τ/A^2 with τ being the local optical depth and A the magnification, an interesting number of detections could be potentially ascribed to microlensing.

A crude estimation of the number of possible γ -ray sources produced by microlensing can be obtained as the product of three factors: *random lensing probability* \times *local lensing probability* \times *number of background sources*, i.e. approximately $5 \times 10^{-3} \times 1/A^2 \times 10^7$. The uncertainty in the previous expression, however, is large. We can only roughly estimate the total number of background sources, but the value of A they need to become visible i.e. with fluxes above the sensibility of EGRET and/or GLAST, will depend on the luminosity function of γ -ray emitting AGNs, which is unknown. According to the different sensitivities of both instruments, we could expect, perhaps, a number of detections of ~ 10 and ~ 100 , respectively.

6.4 Number of events per light curves

We shall now estimate the number of microlensing events expected for a γ -ray blazar with a galaxy interposed in the line of sight. For the galaxy mass distribution we shall adopt the model used by Griest (1991) –see also Eq. (49) above–, where the density profile is given by

$$\rho(r) = \rho_0 \frac{a^2}{a^2 + (x^2 + y^2 + z^2)}, \quad (66)$$

and where ρ_0 is the mass density in the center of the galaxy and a is the core radius of the halo. We shall consider that the entire microlens population is at the same distance from the observer. The projected surface mass density of the microlensing at a radius $r^2 = x^2 + y^2 = \text{constant}$ from the center of the galaxy will be

$$\Sigma(r) = \int_{-\infty}^{\infty} dz \rho_0 \frac{a^2}{a^2 + (x^2 + y^2 + z^2)} = \frac{\pi \rho_0 a^2}{\sqrt{a^2 + r^2}}. \quad (67)$$

Assuming that $\Sigma(r)$ is constant for the smallest impact parameters and equal to $\Sigma_c = \Sigma(r = 0)$, we obtain

$$\Gamma = \frac{\Sigma_c \pi u^2 R_E^2}{M} = B^2 \kappa_s, \quad (68)$$

with $\kappa_s = \Sigma_c / \Sigma_{\text{crit}}$. Usually B is taken as unity. This would happen, for instance, when the distant quasar and the galaxy in which the lenses reside are perfectly aligned (as in the case of PKS 0537-441, see Romero et al. 1995 for discussion). In this case, all lenses are close to the center of the galaxy, and the previous approximation is valid. After some algebra, and taking derivatives, we may write this latter expression as

$$d\Gamma = \frac{d\Sigma_c}{\Sigma_{\text{crit}}} B^2 = \frac{\Sigma_c}{\Sigma_c} \frac{d\Sigma_c}{\Sigma_{\text{crit}}} B^2 = \Gamma \frac{d\Sigma_c}{\Sigma_c}. \quad (69)$$

In order to make further estimates, we need to assume some parameterization for the mass function of the lenses. The standard choice is a power law of the form $N(M) \propto M^{-\alpha}$

(e.g. D’Antona & Mazzitelli 1986). It is likely, however, that a single power law will not suffice for all different types of stars. The value of α , also known as the Salpeter index, is usually taken as 2.35 (Salpeter 1955), although more massive stars may require a steeper index, whereas it could probably be flatter for the less massive stars. As was done in Surpi et al. (1996), we normalize the mass function to yield a total surface density $\Sigma_c = \kappa_s \Sigma_{\text{crit}}$ at the center of the galaxy. The differential surface density in objects with masses between M and $M + dM$ at the center would then be

$$\frac{d\Sigma_c}{\kappa_s \Sigma_{\text{crit}}} = \frac{MN(M)dM}{\int_{M_{\text{min}}}^{M_{\text{max}}} MN(M)dM}. \quad (70)$$

Using this last expression in Eq. (69) we find

$$d\Gamma = \frac{\Gamma}{C(\alpha, M_{\text{min}}, M_{\text{max}})} \left(\frac{M}{M_{\odot}}\right)^{1-\alpha} d\left(\frac{M}{M_{\odot}}\right), \quad (71)$$

with

$$C(\alpha, M_{\text{min}}, M_{\text{max}}) = \frac{\left[\left(\frac{M_{\text{max}}}{M_{\odot}}\right)^{2-\alpha} - \left(\frac{M_{\text{min}}}{M_{\odot}}\right)^{2-\alpha}\right]}{2-\alpha}, \quad \text{for } \alpha \neq 2, \\ = \ln\left(\frac{M_{\text{max}}}{M_{\text{min}}}\right), \quad \text{for } \alpha = 2. \quad (72)$$

Following Subramanian & Gopal-Krishna (1991), if the lenses have the same mass and the observing period is Δt , the expected number of events in the case of a background source moving with velocity v will be

$$N = \Gamma \left(1 + \frac{2\Delta t}{\pi B t_0}\right), \quad (73)$$

where Γ is the optical depth and $B = b/R_E$. Then, using Eq. (71), we obtain

$$dN = \left(\frac{2v\Delta t}{\pi B R_E} + 1\right) \times \frac{\Gamma}{C(\alpha, M_{\text{min}}, M_{\text{max}})} \left(\frac{M}{M_{\odot}}\right)^{1-\alpha} d\left(\frac{M}{M_{\odot}}\right). \quad (74)$$

It is convenient to write the previous expression in more useful units. We define the dimensionless parameter

$$\mathcal{D} = \frac{1}{\pi} \frac{30\text{days}}{\sqrt{GM_{\odot}}} c^2 \sqrt{\frac{D_{os}}{D_{ol} D_{ls}}}, \quad (75)$$

to finally obtain

$$dN = \mathcal{D} \frac{\sqrt{\kappa_s \Gamma}}{C} \frac{\Delta t}{30\text{days}} \frac{v}{c} \left(\frac{M}{M_{\odot}}\right)^{1/2-\alpha} d\left(\frac{M}{M_{\odot}}\right) + \frac{\Gamma}{C} \left(\frac{M}{M_{\odot}}\right)^{1/2-\alpha} d\left(\frac{M}{M_{\odot}}\right). \quad (76)$$

For typical values, say $z_s \sim 0.9$ and $z_l \sim 0.1$, $\mathcal{D} \sim 2.1$. Eq. (76) can now be used to obtain the number of events per lens mass interval as well as the total number of microlensing events.

For the assumed power law mass distribution of lenses between $M_{\text{min}} < M < M_{\text{max}}$, the number of expected microlensing events by stars with masses in the range (M_1, M_2) ,

included in the total mass range $(M_{\text{min}}, M_{\text{max}})$, during Δt days of observations is

$$N_{M_1-M_2}^{\Delta t} = \frac{D(\alpha, M_1, M_2)\Gamma}{C} + 2.16\sqrt{\kappa_s \Gamma} \frac{v}{c} \frac{D(\alpha, M_1, M_2)}{C(\alpha, M_{\text{min}}, M_{\text{max}})} \frac{\Delta t}{30\text{days}}, \quad (77)$$

where D is given by

$$D(\alpha, M_1, M_2) = \frac{2 \left[\left(\frac{M_2}{M_{\odot}}\right)^{\frac{3}{2}-\alpha} - \left(\frac{M_1}{M_{\odot}}\right)^{\frac{3}{2}-\alpha} \right]}{3-2\alpha}, \quad \text{for } \alpha \neq \frac{3}{2}, \\ = \ln\left(\frac{M_2}{M_1}\right), \quad \text{for } \alpha = \frac{3}{2}, \quad (78)$$

and we have assumed the previously mentioned redshifts ($z_s \sim 0.9$ and $z_l \sim 0.1$) to fix the numerical coefficient. Clearly, the total number of events will strongly depend (apart from the expected influence of Γ and κ_s) on the relative source-lens velocity and the Salpeter index α .

Blazars where the bulk of the high-energy emission is produced in a superluminal component with apparent velocity $v > c$ in the lens plane will produce γ -ray sources with the highest levels of variability. In Figure 14 we present three curves showing the total number of microlensing events in a 5 years period for the case of the source being a blazar superluminal component, a subluminal ($v = 0.5c$) component, and for a fixed core source with a foreground lens moving with $v \sim 1/100c$. We find that during the EGRET observing time, and in the case of the lensing of a superluminal source, hundreds of events can be expected.¹ These γ -ray sources can strongly fluctuate from one viewing period to another, leading to high levels of variability. Instead, AGNs whose velocities in the lens plane are much smaller than c will be only mildly affected by lensing, yielding few events for usual values of Γ . These cases would produce γ -ray light curves shifting from detection to upper limits in separated viewing periods, even producing only one γ -ray detection in a period of five years. Depending ultimately on the mass of the lens, this unique event could produce a steady non-variable source (seen along consecutive viewing periods), or one which is seen only during a single viewing period. The peculiarities of each event will ultimately determine the time scales involved. Table 2 shows the results for the total number of events for different lensing parameters, whereas Table 3 shows the distribution of the events by lensing mass. It is interesting to note that most of the events are produced by MACHO-like, sub-stellar mass objects. These objects present small Einstein radius, indicating that only the innermost γ -spheres will be magnified. In addition, this would entail smaller time scales, and within the galactic model here considered, more variable γ -ray sources.

¹ “Events” refers to single spikes within the light curves whereas “sources” to the number of EGRET detections in different parts of the sky that could be ascribed to this mechanism.

Table 2. Total number of events for different lensing parameters and Salpeter indices produced in a period of five years. Two cases (bottom panels) show the results for very low optical depths: even in that cases, significant number of events are expected if the sources have apparently superluminal velocities.

κ_s	Γ	v/c	M_{\min}/M_{\odot}	M_{\max}/M_{\odot}	α	N
0.4	0.2	3.5	0.1	20	1.8	115.1
					2.1	158.8
					2.3	189.9
					2.5	255.1
					3.0	273.9
0.4	0.2	0.016	0.1	20	1.8	0.7
					2.1	0.9
					2.3	1.1
					2.5	1.3
					3.0	1.7
0.4	0.2	0.5	0.1	20	1.8	16.6
					2.1	22.8
					2.3	27.2
					2.5	31.4
					3.0	39.5
0.6	0.2	0.5	0.1	20	1.8	20.3
					2.1	27.9
					2.3	33.5
					2.5	38.6
					3.0	48.2
0.2	0.4	0.9	0.1	20	1.8	29.9
					2.1	41.1
					2.3	49.3
					2.5	56.9
					3.0	71.7
0.4	0.4	0.016	0.1	20	1.8	1.1
					2.1	1.5
					2.3	1.8
					2.5	2.1
					3.0	2.6
0.8	0.6	0.5	0.1	20	1.8	40.8
					2.1	56.2
					2.3	67.2
					2.5	77.5
					3.0	96.9
0.4	0.01	0.01	0.1	20	2.5	0.1
					–	1.4
					–	7.0
					–	48.9
0.4	0.001	0.01	0.1	20	2.35	0.0
					–	0.4
					–	2.0
					–	14.0

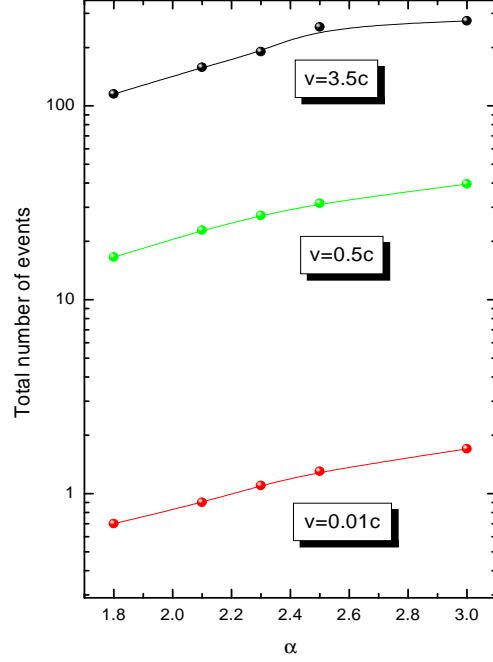


Figure 14. Number of events as a function of the Salpeter index α for the case of apparently super and sub-luminal movements of the source in the lens plane. Lensing parameters are $\gamma = 0$, $\kappa_s = 0.4$, and $\Gamma = 0.2$. For $v \ll c$, the time scale of one event is comparable with EGRET observing time. For $v \sim c$ the time scale of a single event is comparable with one EGRET viewing period.

Table 3. Distribution of the number of lensing events by mass for a galaxy with $\kappa_s = 0.4$, $\gamma = 0$, and $\Gamma = 2$. The Salpeter index is $\alpha = 2.1$ for the first panel, $\alpha = 2.3$ for the second, and $\alpha = 2.5$ for the third one. The relative source velocity in the lens plane is chosen as $v = 3.5c$, $0.1c$ and $0.01c$, from top to bottom.

Mass range (M_{\odot})	$N_{10^{-2}-10^{-1}}^{5\text{years}}$	$N_{10^{-1}-1}^{5\text{years}}$	$N_{1-20}^{5\text{years}}$
1 – 20	–	–	69.4
10^{-1} – 20	–	124.1	347
10^{-2} – 20	303.2	76.1	21.3
1 – 20	–	–	2.2
10^{-1} – 20	–	4.8	0.8
10^{-2} – 20	13.7	2.1	0.4
1 – 20	–	–	0.3
10^{-1} – 20	–	0.8	0.0
10^{-2} – 20	2.6	0.2	0.0

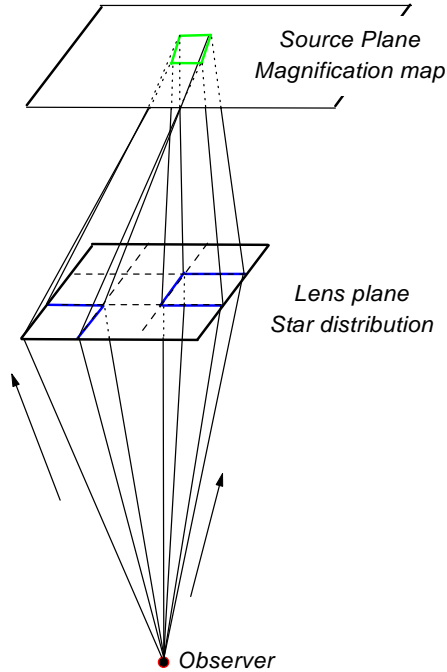


Figure 15. Light rays are traced back towards the source. Each of them is deflected in the lens plane. Different parts of the lens plane can generate deflections converging onto the same pixel in the source plane. There, the magnification map –the number of rays per pixel– is made. Once this is done, a source with a given size moves in this magnification plane and generates a light curve.

6.5 Critical assessment

Although the Chang-Refsdal scheme used in the previous section is a very important tool in the understanding of the model herein proposed, it cannot be used to claim precise predictions for the magnifications. For high values of κ_s and γ a more complex caustic pattern should be considered in order to get reliable light curves and the correct magnifications. The quantitative predictions for the amount of magnification and the form of the light curves could actually change in more detailed simulations of a galaxy core (where the effects of thousands of stars are considered simultaneously). The rest of this paper is devoted to develop full numerical models of the situation presented from an analytical point of view in the previous sections .

7 MAGNIFICATION MAPS

As we have seen, the parameters that describe a microlensing scenario are the dimensionless surface mass density κ –expressed in units of the critical surface mass density– and the external shear γ (cf. Kayser, Refsdal & Stabell

1986; Schneider & Weiss 1987). The former –often also called convergence or optical depth– describes the amount of matter in front of the source. The latter is a tidal force caused by matter outside the light bundle. In order to simulate the effect of a particular combination of κ and γ , point lenses are distributed randomly according to the given surface mass density. If we would replace each point lens by a disk with radius equal to its Einstein radius, the total fraction of the sky that is covered by the sum of all these disks is equal to the optical depth.

For the ray-shooting simulations, a large number of light rays (of order 10^9) are followed *backwards* from the observer through the field of point lenses. The number of rays determine the resolution of the numerical simulation. These rays start out in a regular (angular) grid. In the lens plane, the deflections according to the individual lenses are then superposed for each individual ray i ,

$$\bar{\alpha}_i = \sum_{j=1}^n \bar{\alpha}_{ij} = \frac{4G}{c^2} \sum_{j=1}^n M_j \frac{\bar{r}_{ij}}{r_{ij}^2}. \quad (79)$$

Here M_j is the mass of the point lens j , \bar{r}_{ij} is the projected vector distance between the position of the light ray i and the lens j , and r_{ij} is its absolute value. It is the computations of these individual deflections what requires most of the time of the simulation. The effect of the external shear is included as well. The deflected rays are then followed further to the source plane. There, they are collected in small pixels. The number of rays per pixel (on average ~ 100 for a region typically of 2500×2500 pixels) is proportional to the magnification at this position. A two-dimensional map of the ray density –a magnification pattern, also referred to as caustic pattern– can then be produced. The magnification as a function of (source) position is indicated by colors. Sharp lines correspond to locations of very high magnification, i.e. the caustics. In Figure 15 we schematically show the geometry of the shooting technique.

The minimal number of lenses that have to be considered depends on the focusing and shear values, as well as on the ratio between the diffuse and the total flux. The diffuse flux (ϵ) is that coming from rays that are deflected into the receiving area from stars far outside the region where microlenses are considered, and should be consistently low. An approximated expression for the number of lenses to be included in each magnification map is (Wambsganss 1999)

$$N_* \sim \frac{3\kappa^2}{(1-\kappa)^2 - \gamma^2} \frac{1}{\epsilon} \quad (80)$$

which entails values from several hundreds (for $\kappa < 0.4$) up to several hundred thousands (for $\kappa \sim 1$) stars, in the case of zero shear and $\epsilon = 0.01$. Since for computing the map with high resolution, this would imply literally several million billions of operations, an intelligent numerical routine should come to the rescue to make this problem feasible. The technique is called hierarchical tree code. Basically, it groups the stars as a function of their distance

to the light ray. Since their influence decreases as gravity does, with r^{-2} , one does not need to compute the deflection from all the stars involved with the same level of precision to obtain an overall sensitive result. A detailed account of the numerical technique can be found in the paper by Wambsganss (1999).

In general, a smooth out distributed surface mass density κ_c also contributes to the deflection as well, and the general microlensing equation to be solved is

$$y = \begin{pmatrix} 1 - \kappa - \gamma & 0 \\ 0 & 1 - \kappa + \gamma \end{pmatrix} \bar{x} - \kappa_c \bar{x}. \quad (81)$$

In observational situations κ_c and γ are obtained from macrolensing simulations of the resolved source. Rays representing a square ($x_1 = x_2$) are then mapped onto a rectangle with a side ratio $T = (1 - \kappa - \kappa_c - \gamma)/(1 - \kappa - \kappa_c + \gamma)$. But, as we would like the receiving –and not the shooting– area to be a square (the pixel) the shooting field (i.e. the area in the lens plane in which rays are mapped) is chosen to be a rectangle of size T^{-1} .

The fact that source, lens and, observer are moving relative to each other, means that the source is affected by a variable magnification as a function of time: it moves through the magnification pattern and so we measure a variable flux. When a source crosses a caustic, formally two very bright new (micro-)images appear or disappear. However, their angular separation is much smaller than the resolution of any telescope. Therefore, we can only measure the combined total brightness, which can produce dramatic ‘jumps’ in the observed flux. Assuming geometrical optics and a point source, the amount of the magnification is infinite. However, since any real source is finite, the magnification stays finite as well. The exact amount of magnification depends on the source size: the smaller it is, the higher the magnification. In order to determine the light curve for a finite source, its brightness profile has to be convolved with this two-dimensional magnification pattern.

7.1 Results of the numerical simulations

In Figure 16 we show the magnification map for the case in which $\kappa = 0.5$ and $\gamma = 0.0$; the brighter the region, the stronger the magnification. The characteristic critical lines of the Chang-RRefsdal model appear in this map, as well as the diamond shaped structures due to the close-by star. In the bottom left of the panel, we show the size of the source for three different energies. The innermost pixel (the center of the circles) represent the size of the lowest energy γ -sphere, that corresponds to $E = 100$ MeV. The second circle is the size of the 1 GeV γ -sphere, whereas the largest one is the corresponding size of the $E = 10$ GeV emitting region. It is clear the origin of the differential magnification: the γ -spheres will be affected according to their size while moving in the caustic pattern.

The numbered lines in Figure 16 represent different

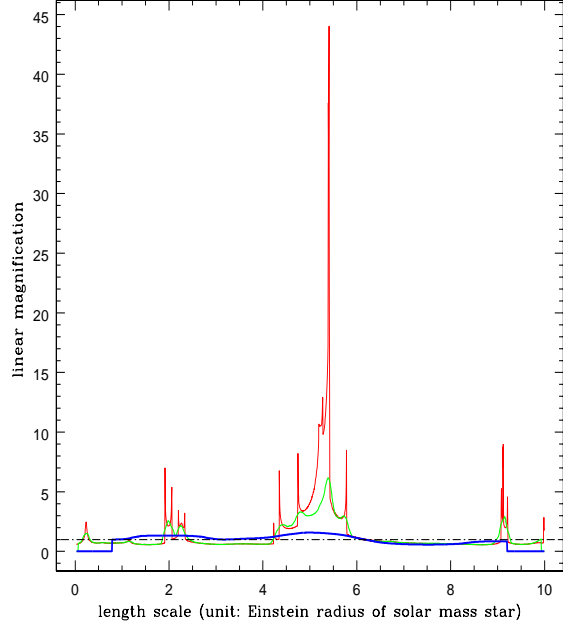


Figure 18. Light curve for trajectory number 7, producing one of the highest levels of magnification out of map given in Figure 16. The line coding is as in Figure 17.

source trajectories. Numbers 1 to 6 are trajectories common to all maps we shall present, and are defined a priori in our code. The light curves for each of these six trajectories are given in Figure 17. We can see that the overall effect described with the Chang-RRefsdal model appears here as well. In lighter color we show, for each trajectory, the corresponding light curve for the $E = 100$ MeV emitting region. Darker lines correspond to regions emitting photons of 1 and 10 GeV. The latter, in all cases, are smoother versions of the former and, always, the magnification is weaker for these regions. There is a typical factor of 10 more magnification for the innermost regions than for the larger γ -spheres. We see that for these values of κ and γ it is possible to get a typical enhancement of 10 times the unlensed intensity at 100 MeV. The drop to zero at the corners of the diagram for all light curves corresponding to the largest γ -sphere is an artifact of the simulations: the code assigns zero magnification when more than half of the source is out of the magnification map.

The shape of the light curves is also worthy to comment. As an example, we take trajectory 3. It starts in a region of low magnification and continues upwards, crossing a region of relatively high enhancement, where for the innermost γ -sphere the magnification is 9 times the intensity of the unlensed source. There are four caustic crossings there. We can see that for the innermost γ -sphere, the caustic crossings are well separated events, so we have four peaks in the light curve corresponding to $E = 100$ MeV. However, for the larger γ -spheres the peaks are smoothed down. We

Figure 16. Magnification map for lensing with parameters $\kappa = 0.5$ and $\gamma = 0.0$. For details, see text. The corresponding file is *magpat κ 50g00.gif*.

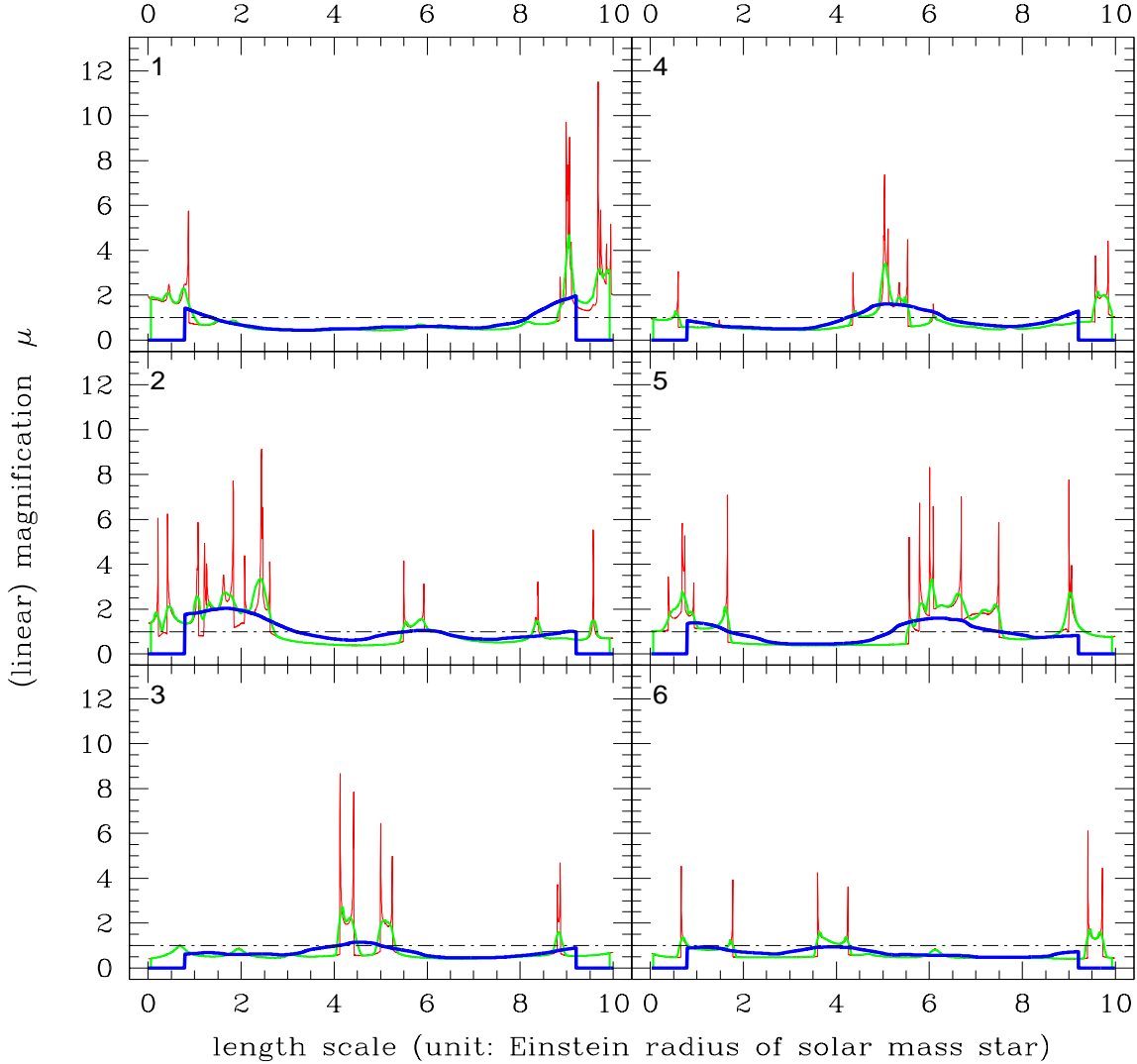


Figure 17. Light curves for different source trajectories. Numbers corresponds to those given in Figure 16. Darker lines corresponds, respectively, to regions emitting photons of 100 MeV, 1, and 10 GeV, and whose emitting sizes are depicted in the bottom left corner of Figure 16, being the innermost point the less energetic γ -ray sphere.

see only two broadened peaks for $E = 1$ GeV, and only one, with almost nil magnification, in the case of $E = 10$ GeV. If the γ -ray AGN is within the observing sensitivity, we would see a distinctive effect during the microlensing event due to the different sizes of the source at the different energies.

The x -axis in Figure 17 is a linear length scale, the Einstein radius of a solar mass star, $R_E(M_\odot) = 2.23 \times 10^{16}$ cm. It can be translated into a time scale as $t = R_E(M_\odot)/v$,

where v is the relative velocity of the source with respect to the lens, projected onto the source plane. Typical time scales for microlensing events where discussed in Section 6.1. To give an example of the similar time scales predicted with a full caustic pattern plot, we write the time scale as

$$t = \frac{R_E(M_\odot)}{v} = \frac{0.023}{v/c} \text{yr}. \quad (82)$$

With a relative velocity $v = 5000$ km s^{-1} , the length of each axis in Figure 16 is equivalent to 14 years. The other

important time scale involved in a microlensing event is the rise time to a peak of maximum magnification. This will depend on the size of the different γ -spheres, and is given by

$$\tau = \frac{R}{v} = \frac{0.023}{v/c} \frac{R}{R_E(M_\odot)} \text{yr}, \quad (83)$$

where, again, we have scaled it with the Einstein radius corresponding with one solar mass. Then, the innermost γ -spheres (having $R/R_E \sim 1/100$) will have a rise time scale of about 5 days, well within an observing EGRET viewing period. The largest γ -spheres, with $R \sim R_E$, can have a rise time of about 1 yr. Higher (lower) velocities would imply lower (higher) time scales.

In order to explore the maximum possible magnification that this caustic pattern produces, we have selected an extra trajectory that crosses exactly over a conjunction of several caustics (trajectory 7 in Figure 16). The light curve is separately shown in Figure 18. We can see that magnifications up to 45 times the unlensed intensity of the source are possible in this configuration. The effect of the differential enhancement is notoriously clear for this case.

In Figure 19 we show the magnification map corresponding to a higher value of focusing, $\kappa = 0.8$. Still in this case, the shear γ is taken equal to zero. As it was found by Schneider & Weiss (1987), the critical structure become more complex with increasing κ and is no longer possible to identify a constellation of compact objects. In addition, we also see (as in Figure 16) the tendency of the caustic structure to cluster, generating some crowded critical regions and some others devoid of high magnification patterns. The explanation for this was already given by Schneider & Weiss (1987): The clustering of caustics is just the non-linear enhancement of random (Poisson) clustering of the positions of lenses in the source plane. Over-dense regions tend to attract other over-dense regions, because gravity is a long range force.

The most important feature shown in the map of Figure 19 is that the magnitude of the magnification has been typically reduced with respect to the $\kappa = 0.5$ case, and this reduction reach two orders of magnitude with respect to the single events. The density of caustics is so large that the light curve is continuously affected by them, producing a less dramatic combined effect. This effect was first studied by Deguchi & Watson (1987): The total magnification is always high, but the fluctuations decreases beyond $\kappa = 0.5$. This effect can be seen in the light curves presented in Figure 20. Even for the particularly chosen trajectory, number 7, we find a maximum magnification of 7. The full light curve is presented in Figure 21. Again, the differential effect is notorious.

In Figure 22 we show the magnification pattern for the case $\kappa = 0.2$ and $\gamma = 0.16$. The presence of shear modifies qualitative the magnification map. Here, most of the map is devoid of magnification, and so, many of the common trajectories (numbers 1 to 6) cross large regions of very low

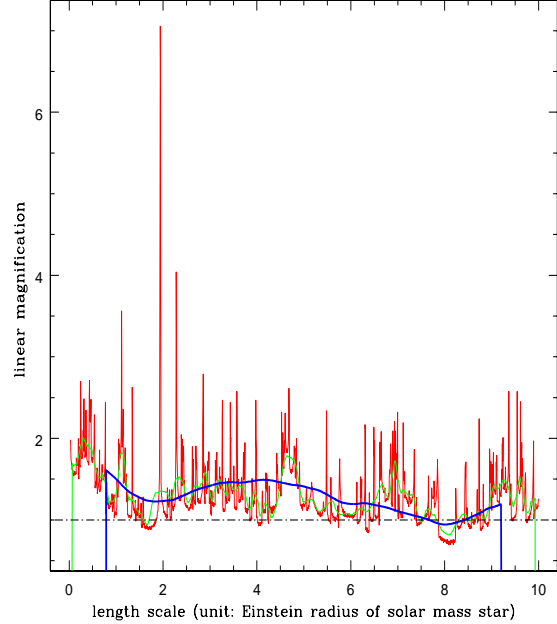


Figure 21. Light curve for trajectory number 7, producing one of the highest levels of magnification out of map given in Figure 19. The line coding is as in Figure 17.

or nil magnification (see particularly trajectory 6). However, those trajectories actually crossing the caustics produce enhancements in intensity typically between 10 and 20 times the unlensed value. These effects can be seen in the six panels of Figure 23, where the differential magnification for the different γ -spheres is also noticeable. In addition, the enhancements of intensity are usually well separated (see for instance trajectory 4). The enhancements themselves are reminiscent of those produced by single events considered in Section 6, in those cases where the presence of shear was significant.

From the point of view of unidentified γ -ray sources, interposed galaxies with low values of κ and γ are probably the most interesting case for the application of the model. In Figure 24 we show the case for the hand-selected light curve. In that case, the magnification reaches a factor of 65. The probability for this trajectory is less than those of average enhancement. However, even if the probability is reduced by, say, a factor $1/A^2$, it is possible to expect many cases of high magnification, like that presented in Figure 24.

Finally, in Figure 25 we show the magnification map corresponding to the case $\kappa = 0.9$ and $\gamma = 0.4$. Again, the high value of κ makes the critical structure highly complex. Typically, the magnification values are below a factor of 10 of the unlensed intensity, although some trajectories are found (see, for example, curves number 3 and 4 of Figure 26) where a factor of ~ 10 is reached in two well separated regions.

Figure 19. Magnification map for lensing with parameters $\kappa = 0.8$ and $\gamma = 0.0$. For details, see text. The corresponding file is *magpat κ 80g00.gif*.

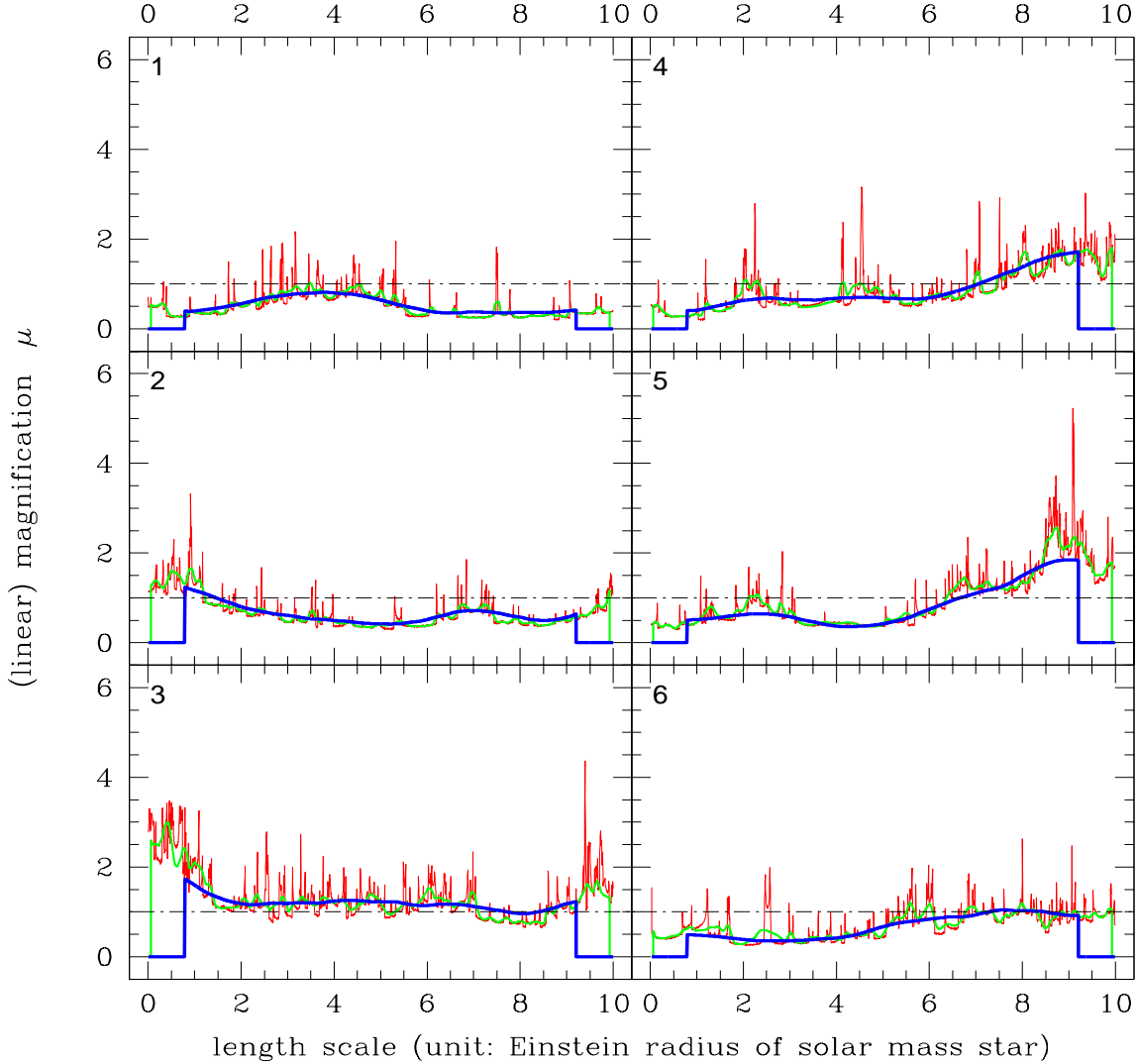


Figure 20. Light curves for different source trajectories. Numbers corresponds to those given in Figure 19. The line coding is as in Figure 17.

Trajectory 7 (whose light curve is given in Figure 18) shows an enhancement of 22 times the unlensed intensity.

7.2 Speculations on astrophysical applications

Let us assume that a correct alignment of source, lens, and observer has been produced and that microlensing is operative. A possible astrophysical application of the effects we have discussed in the previous sections is to constrain the exponent in the relationship between size and energy for γ -

ray spheres in the AGNs, $R \propto E^\alpha$. The smaller the source, the higher is the peak γ -ray luminosity, and shorter will result the rise time scale ($\tau = R/v$). Therefore, by observing throughout the peak at different energies, one could determine the relative size of the source at such energies, and then test the radius–energy theoretical relationship. This could be done within the range of GLAST capabilities. If, somehow, we know the relative velocity and the redshifts, we could in even determine the sizes of the different emitting regions.

Figure 22. Magnification map for lensing with parameters $\kappa = 0.2$ and $\gamma = 0.16$. For details, see text. The corresponding file is *magpat κ 20 γ 16.gif*.

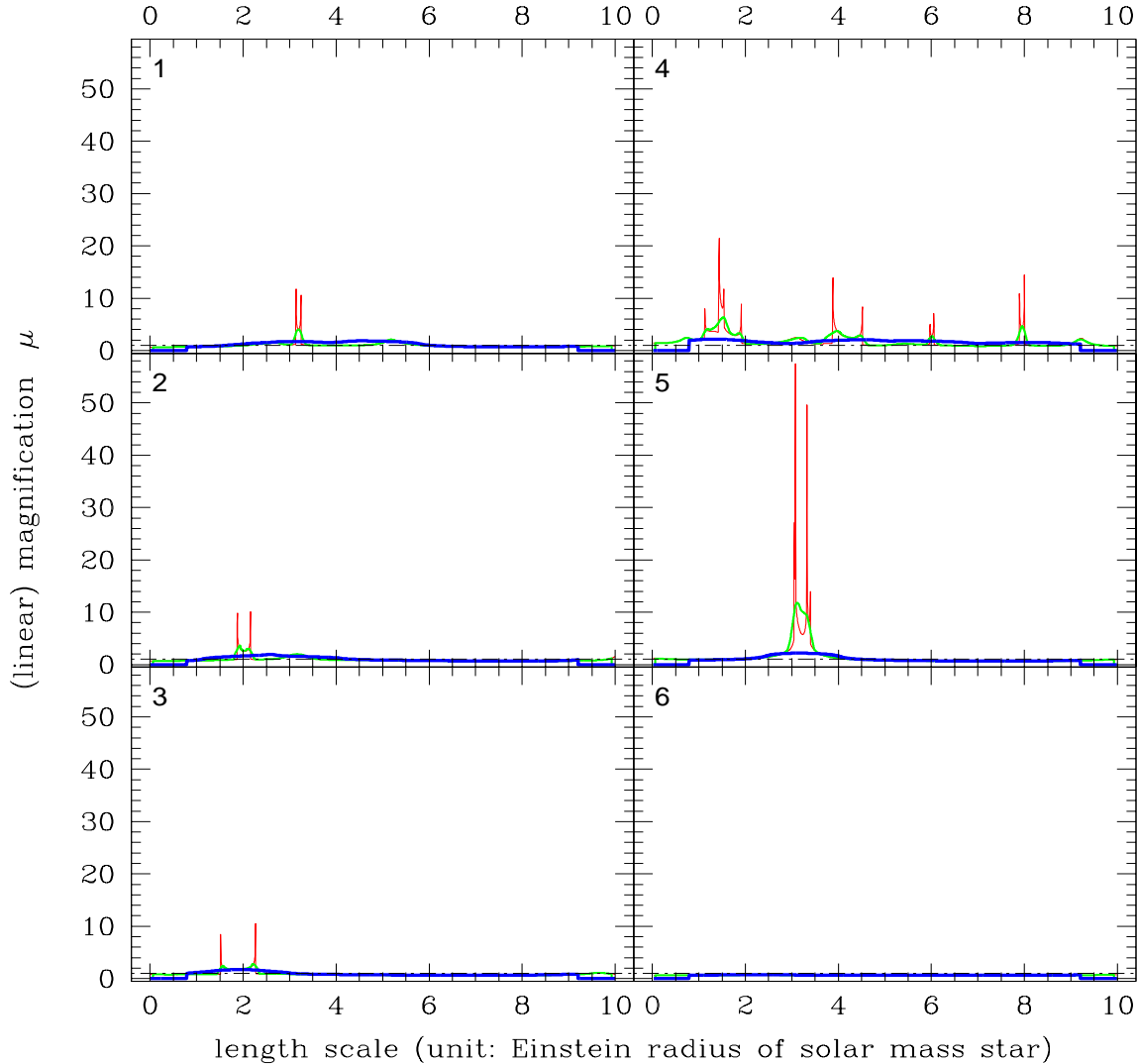


Figure 23. Light curves for different source trajectories. Numbers corresponds to those given in Figure 22. The line coding is as in Figure 17.

This would directly impact on the underlying γ -ray models (e.g. Becker & Kafatos 1995, Blandford & Levinson 1995).

8 SUMMARY AND FINAL COMMENTS

To summarize, we have shown in this paper that

- Some of the high-latitude unidentified γ -ray sources (both variable and non-variable) could be weak γ -ray emitting AGNs that are magnified through gravitational

microlensing by stars in foreground galaxies.

- Although small, the probability of gravitational microlensing could be enough to explain a handful of the EGRET detections, and maybe many of the forthcoming GLAST detections.

- During a γ -ray variability event produced by microlensing of a blazar, there is a peculiar spectral evolution that could be detected in principle by the next generation of γ -

Figure 25. Magnification map for lensing with parameters $\kappa = 0.9$ and $\gamma = 0.4$. For details, see text. The corresponding file is *magpat κ 90 γ 40.gif*.

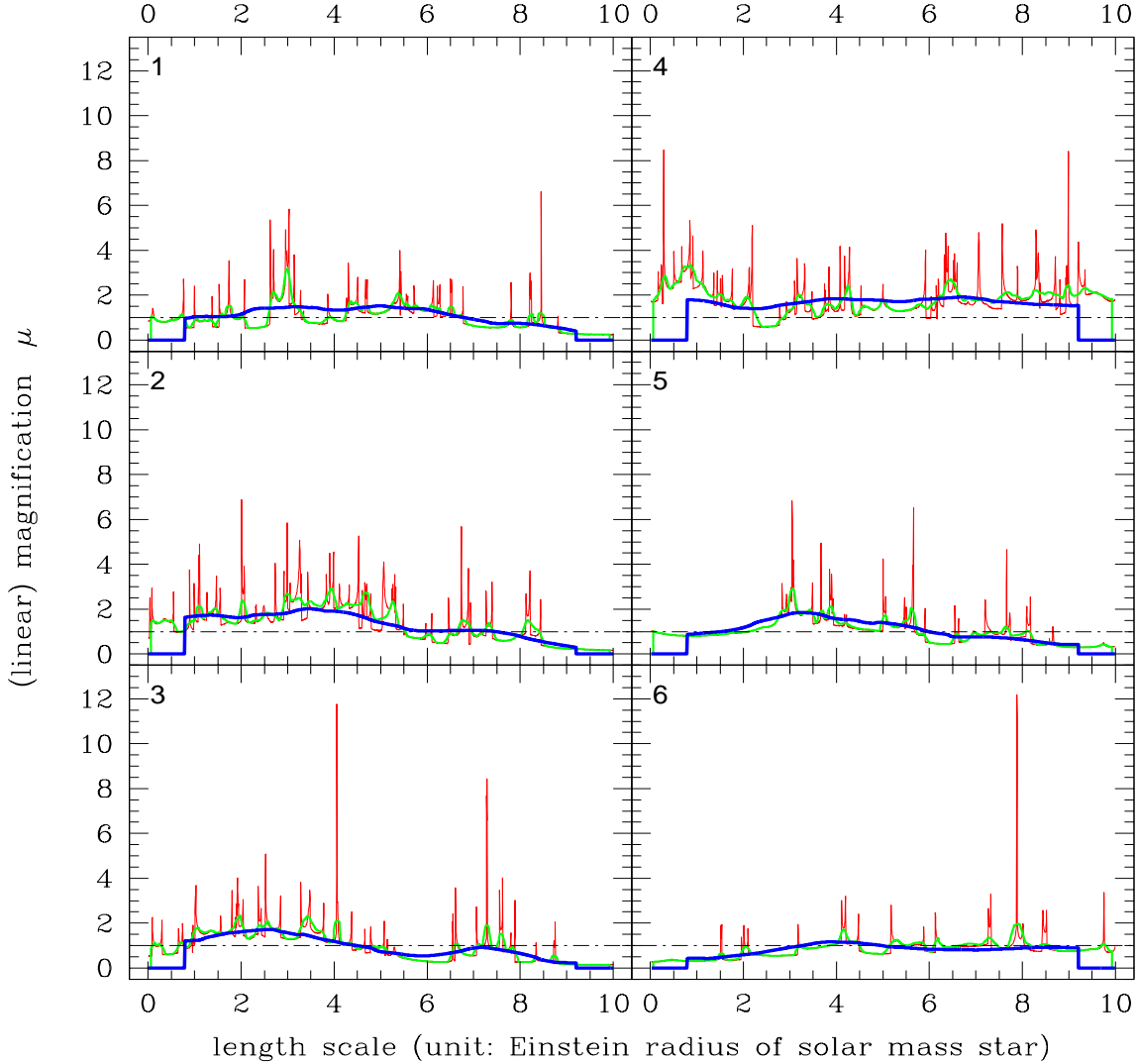


Figure 26. Light curves for different source trajectories. Numbers corresponds to those given in Figure 25. The line coding is as in Figure 17.

ray observatories with fine spectral capabilities, like GLAST, or even by ground γ -ray telescopes located at sufficient altitude, like 5@5 (e.g. Aharonian et al. 2001).

It should be clearly stated that this model can not account for all unidentified γ -ray detections at high latitudes. However, it is interesting to ask whether the proposed microlensing scenario could be responsible for γ -ray variability of some radio loud AGNs already detected by EGRET. Indeed, there is one possible case, related with the source 3EG J1832-2110, which has been identified with PKS 1830-211

(Mattox et al. 1997, Combi & Romero 1998). The latter is a flat-spectrum radio source, proposed to be a gravitational lensed QSO by Pramesh Rao & Subrahmanyam (1988). The γ -ray source is likely variable, presenting a value of $I = 2.5$, and a steep spectral index, $\Gamma = 2.59 \pm 0.13$. Both facts, variability and a steep spectra, argue against a galactic origin for this source. Mattox et al. (2001) assign to this pair an a priori probability of 0.998 of being correct, and list it within the most likely AGN identification of the Third

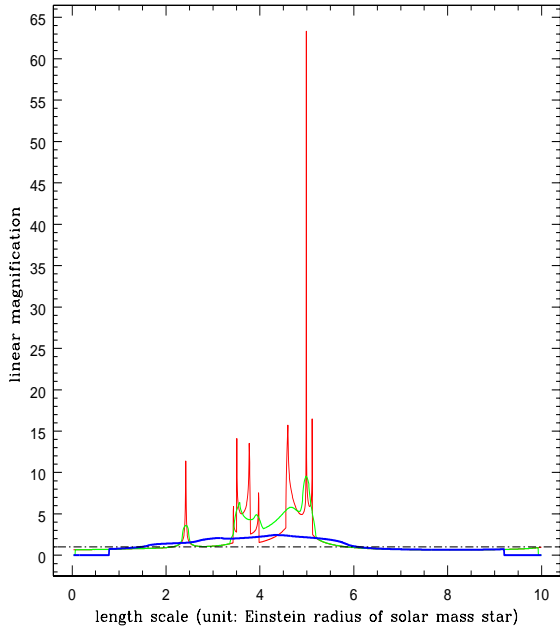


Figure 24. Light curve for trajectory number 7, producing one of the highest levels of magnification out of map given in Figure 22. The line coding is as in Figure 17.

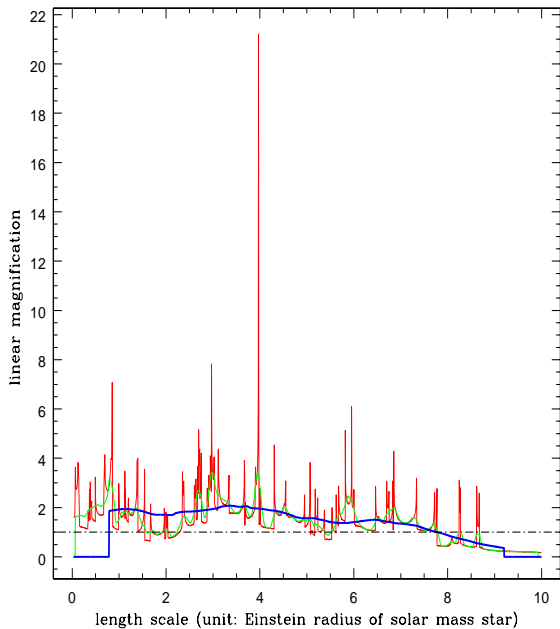


Figure 27. Light curve for trajectory number 7, producing one of the highest levels of magnification out of map given in Figure 25. The line coding is as in Figure 17.

EGRET Catalog.

High resolution radio images obtained from several interferometric arrays have revealed that the source has a ring-like structure with two bright components on sub-arcsecond scales (Jauncey et al. 1991). This suggests a close alignment of the lensed source behind the lensing object. Two absorption systems have been detected at $z \sim 0.89$ (Wiklind & Combes 1996) and $z \sim 0.193$ (Lovell et al. 1996), so it seems likely that the image of the background QSO (with a redshift $z > 0.885$, Mattox et al. 2001) is lensed by two different extragalactic objects, what would undoubtedly enhance the optical depth and the number of expected single microlensing events.

Indeed, Combi & Romero (1998) have already proposed that the γ -ray emission of 3EG J1832-2110 (then 2EG J1834-2138) could be produced by gravitational microlensing, using exactly the same ideas we have deepen in this paper. They have found that assuming a redshift $z_s = 1$ for the background source and $z_l \sim 0.89$ for the lens, a MACHO-like object with $M \sim 0.02M_\odot$ and moving with a low velocity of only $v \sim 1000 \text{ km s}^{-1}$ would be enough to produce the observed variability. For this to be possible, the size of the γ -ray emitting region should be of about $1.5 \cdot 10^{15} \text{ cm}$, in good agreement with the source sizes used in this paper. These results can be slightly modified by new measurements of the quasar redshift, but will not change substantially (Oshima et al. 2001).

It is likely then that the first realization of this proposed mechanism have been already observed for the pair 3EG J1832-2110/PKS 1830-211. One thing should be remarked, though: in this case the background source is already a strong radio emitter –what indeed facilitates the identification–. This was not the general case we have considered here, where the sources are weak enough as to yield no significant lower energy counterparts. A complete microlensing model for the γ -ray variability of PKS 1830-211, based on the discussion presented in this paper, will be presented in a forthcoming publication.

ACKNOWLEDGMENTS

This work has been supported by Universidad de Buenos Aires (UBACYT X-143, EFE), CONICET (DFT, and PIP 0430/98, GER), ANPCT (PICT 98 No. 03-04881, GER), Princeton University (DFT) and Fundación Antorchas (through separates research grants to GER and DFT). GER was on leave from IAR during part of this research. We acknowledge insightful comments by Drs. E. Turner, R. Hartman, and D. Thompson in an early stage of this research.

APPENDIX: SOLUTIONS TO THE 1D LENS EQUATION

Replacing Eqs. (26) and (27) in Eq. (28) we obtain

$$A_0 = \frac{1}{|1 - \kappa|} \left(\frac{\left(\frac{\varepsilon Y}{2} + \sqrt{\frac{Y^2}{4} + \varepsilon} \right)^4}{\left| \left(\frac{\varepsilon Y}{2} + \sqrt{\frac{Y^2}{4} + \varepsilon} \right)^4 - 1 \right|} + \frac{\left(\frac{\varepsilon Y}{2} - \sqrt{\frac{Y^2}{4} + \varepsilon} \right)^4}{\left| \left(\frac{\varepsilon Y}{2} - \sqrt{\frac{Y^2}{4} + \varepsilon} \right)^4 - 1 \right|} \right), \quad (84)$$

and

$$A_0 = \frac{1}{|1 - \kappa|} \left(\frac{(\varepsilon Y + \sqrt{Y^2 + 4\varepsilon})^4}{\left| (\varepsilon Y + \sqrt{Y^2 + 4\varepsilon})^4 - 16 \right|} + \frac{(\varepsilon Y - \sqrt{Y^2 + 4\varepsilon})^4}{\left| (\varepsilon Y - \sqrt{Y^2 + 4\varepsilon})^4 - 16 \right|} \right). \quad (85)$$

Let us now analyze different situations, starting with the case $\varepsilon = 1, Y > 0$. For it we get,

$$A_0 = \frac{1}{|1 - \kappa|} \left(\frac{(Y + \sqrt{Y^2 + 4})^4}{(Y + \sqrt{Y^2 + 4})^4 - 16} + \frac{(Y - \sqrt{Y^2 + 4})^4}{16 - (Y - \sqrt{Y^2 + 4})^4} \right). \quad (86)$$

If we have the case $\varepsilon = 1, Y < 0$, we get

$$A_0 = \frac{1}{|1 - \kappa|} \left(\frac{(Y + \sqrt{Y^2 + 4})^4}{16 - (Y + \sqrt{Y^2 + 4})^4} + \frac{(Y - \sqrt{Y^2 + 4})^4}{(Y - \sqrt{Y^2 + 4})^4 - 16} \right) \quad (87)$$

For the case in which $\varepsilon = -1, Y > 2$, the magnification results in

$$A_0 = \frac{1}{|1 - \kappa|} \left(\frac{(-Y + \sqrt{Y^2 - 4})^4}{16 - (-Y + \sqrt{Y^2 - 4})^4} + \frac{(-Y - \sqrt{Y^2 - 4})^4}{(-Y - \sqrt{Y^2 - 4})^4 - 16} \right). \quad (88)$$

And lastly, for the case in which $\varepsilon = -1, Y < -2$,

$$A_0 = \frac{1}{|1 - \kappa|} \left(\frac{(-Y + \sqrt{Y^2 - 4})^4}{(-Y + \sqrt{Y^2 - 4})^4 - 16} + \frac{(-Y - \sqrt{Y^2 - 4})^4}{16 - (-Y - \sqrt{Y^2 - 4})^4} \right). \quad (89)$$

The four cases can be jointly written as

$$A_0 = \frac{1}{|1 - \kappa|} sg(Y) \varepsilon \left(\frac{(\varepsilon Y + \sqrt{Y^2 + 4\varepsilon})^4}{(\varepsilon Y + \sqrt{Y^2 + 4\varepsilon})^4 - 16} + \frac{(\varepsilon Y - \sqrt{Y^2 + 4\varepsilon})^4}{16 - (\varepsilon Y - \sqrt{Y^2 + 4\varepsilon})^4} \right). \quad (90)$$

Simplifying the expression between the parentheses, we have

$$\frac{(\varepsilon Y + \sqrt{Y^2 + 4\varepsilon})^4}{(\varepsilon Y + \sqrt{Y^2 + 4\varepsilon})^4 - 16} + \frac{(\varepsilon Y - \sqrt{Y^2 + 4\varepsilon})^4}{16 - (\varepsilon Y - \sqrt{Y^2 + 4\varepsilon})^4} = \frac{\varepsilon Y^2 + 2}{Y \sqrt{Y^2 + 4\varepsilon}}. \quad (91)$$

Then (using that $\varepsilon^2 = 1$), we obtain

$$A_0 = \frac{1}{|1 - \kappa|} sg(Y) \frac{Y^2 + 2\varepsilon}{Y \sqrt{Y^2 + 4\varepsilon}} = \frac{1}{|1 - \kappa|} \frac{Y^2 + 2\varepsilon}{sg(Y) Y \sqrt{Y^2 + 4\varepsilon}}, \quad (92)$$

and as $sg(Y)Y = |Y|$, Eq. (29) follows.

REFERENCES

- Aharonian F.A., Konopelko A.K., Völk H.J., Quintana H. 2001, *Astrop. Phys.* 15, 335
 Benaglia P., Romero G.E., Stevens I. and Torres D.F. 2001, *A&A*, 366, 605
 Becker P., & Kafatos M. 1995, *ApJ* 453, 83
 Blandford R.D., & Levinson A. 1995, *ApJ* 441, 79
 Butt Y.M., Torres D.F., Combi J.A., Dame, T., & Romero, G.E. 2001, *ApJ* 561, L203
 Camilo, F., et al. 2001, *ApJ*, 557, L51
 Chang K., & Refsdal S. 1984, *A&A* 132, 168
 Combi J.A. & Romero G.E. 1995, *A&A* 303, 873
 Combi J.A., & Romero G.E. 1998, *A&AS* 128, 423
 Combi J.A., Romero G.E., & Benaglia P. 1998, *A&A*, 333, L91
 Combi J.A., Romero G.E., Benaglia P., & Jonas, J. 2001, *A&A*, 366, 1047
 Corrigan R.T., Irwin M.J., Arnaud J., et al. 1991, *AJ* 102, 34
 D'Amico, N., et al. 2001, *ApJ*, 552, L45
 D'antona F., & Mazzitelli I. 1986, *AA* 162, 80
 Deguchi S., & Watson W. D. 1987, *Phys. Rev. Lett.* 59, 2814
 Eiroa E. F., Romero G. E., & Torres D. F. 2001, *Mod. Phys. Lett.* A16, 973
 Esposito J.A., Hunter S.D., Kanbach G., & Sreekumar P. 1996, *ApJ*, 461, 820
 Garnavich P.M., Loeb A., & Stanek, K.Z. 2000, *ApJ* 544, L11
 Gehrels N., Michelson P. 1999, *Astrop. Phys.* 11, 277
 Gehrels N., Macomb D.J., Bertsch D.L., Thompson D.J., & Hartman R.C. 2000, *Nature* 404, 363
 Grenier I. 2000, *A&A* 364, L93
 Griest K. 1991, *ApJ* 366, 412
 Han C., Park S-H., & Jeong J-H. 2000, *MNRAS* 316, 97
 Hartman, R.C., et al. 1999, *ApJS*, 123, 79
 Jauncey D.L., Reynolds J.E., Tzioumis A.K., et al. 1991, *Nature* 352, 132
 Kaspi V.M., Lackey J.R., Mattox J., Manchester R.N., Bailes M., & Pace R. 2000, *ApJ*, 528, 445
 Kayser, R., Refsdal, S., Stabell, R. 1986, *A&A* 166, 36

- Kaufman Bernadó M.M., Romero G.E., Mirabel I.F., 2002 *A&A* 385, L10
- Koopmans L.V.E., & de Bruyn A.G. 2000, *A&A* 358, 793
- Koopmans L. V. E., & Wambsganss J. 2001, *MNRAS* 325, 1317
- Krolik J.H. 1999, *Active Galactic Nuclei*, (Princeton University Press, Princeton)
- Lovell J.E.J., Reynolds J.E., Jauncey D.L., et al. 1996, *ApJ* 472, L5
- Mao S., & Loeb A. 2001, *ApJ* 547, L97
- Mattox J.R., Schachter J., Molnar L., Hartman R. C., & Patnaik A. R. 1997, *ApJ* 481, 95
- Mattox J.R., Hartman R.C., & Reimer O. 2001, *ApJS* 135, 155
- Mukherjee R. 2001, in: *High Energy Gamma-Ray Astronomy*, F.A. Aharonian, H.J. Völk (Eds.) (AIP, Melville NY, p.324), astro-ph/0101301
- Oshima T., Mitsuda K., Ota N., Yonehara A., Hattori M., Mihara T., & Sekimoto Y. 2001, *ApJ* 551, 929
- Ostriker J., & Vietri M. 1985, *Nature* 318, 446
- Özel M.E., & Thompson D.J. 1996, *ApJ* 463, 105
- Paczynski B. 1986, *ApJ* 304, 1
- Paczynski B. 1996, *ARAA* 34, 419
- Paredes J. M., Marti J., Ribo M., & Massi M. 2000, *Science*, 288, 2340
- Pramesh Rao A., Subrahmanyan R. 1988, *MNRAS* 231, 229
- Punsly B. 1998a, *ApJ* 498, 640
- Punsly B. 1998b, *ApJ* 498, 660
- Punsly B., Romero G.E., Torres D.F., & Combi J.A. 2000, *A&A*, 364, 556
- Reimer O. 2001, in: *The Nature of Galactic Unidentified Gamma-ray Sources*, O. Carramiana, O. Reimer, D. Thomson (Eds.) (Kluwer Academic Press, Dordrecht, p.17), astro-ph/0102495
- Reimer O., & Thompson D. J. 2001, *Proceedings of ICRC*, in press (astro-ph/0108348).
- Romero G.E., Surpi G. & Vucetich H. 1995, *A&A* 301, 641
- Romero G.E., Benaglia P., & Torres D.F. 1999, *A&A*, 348, 868
- Romero G.E., Chajet L., Abraham Z., & Fan J.H. 2000, *A&A* 360, 57
- Romero G.E., Kaufman Bernadó M.M., Combi J.A., & Torres D.F. 2001, *A&A* 376, 599
- Romero G.E. 2001, in: *The Nature of Galactic Unidentified Gamma-ray Sources*, O. Carramiana, O. Reimer, D. Thomson (Eds.) (Kluwer Academic Press, Dordrecht, p.65), astro-ph/0012243
- Safonova M., Torres D.F. & Romero G.E. 2002, "Microlensing by natural wormholes: Theory and simulations," *Phys. Rev. D* 65, 023001
- Salpeter E.E. 1955, *ApJ* 121, 161
- Schlickeiser R. 1996, *A&AS* 120, 481
- Schneider P., & Weiss A. 1987, *A&A* 171, 49
- Schneider P., Ehlers J., & Falco E.E. 1992, *Gravitational lenses* (Springer-Verlag, Berlin)
- Schneider D.P., Turner E.L., Gunn J.E., et al. 1988, *AJ* 95, 1619
- Subramanian K., & Krishna G. 1991, *A&A* 248, 55
- Surpi G., Romero G.E., & Vucetich H. 1996, *Revista Mexicana de Astronomía y Astrofísica*, 32, 153
- Sturmer S.J., Dermer C.D., & Mattox J.R. 1996, *A&AS*, 120, 445
- Swanenburg B.N., Bennet K., Bignami B.F., et al. 1978, *Nat* 275, 298
- Thompson D.J. 2001, in: *High Energy Gamma-Ray Astronomy*, F.A. Aharonian, H.J. Völk (Eds.) (AIP, Melville NY, p.103), astro-ph/0101039
- Thompson D.J., et al. 1999, *ApJ*, 516, 297
- Tompkins W. 1999, Ph.D. Thesis, Stanford University
- Torres D.F., Romero G.E., Combi J., Benaglia P., Andernach H. & Punsly B. 2001a, *A&A*, 370, 468
- Torres D.F., Combi J.A., Romero G.E., & Benaglia P. 2001b, *Proc. Int. Workshop on The Nature of Galactic Unidentified Gamma-ray Sources*, O. Carramiana, O. Reimer, D. Thomson (Eds.) (Kluwer Academic Press, p.97), astro-ph/0012160.
- Torres D.F., Pessah M.E., & Romero G.E. 2001c, *Astron. Nachr.* 322, 223
- Torres D.F., Butt Y.M. & Camilo F. 2001d, *ApJ Lett*, *ApJ* 569, 600
- Torres D.F., Romero G.E. & Eiroa E.F. 2002a, *ApJ* 569, 600
- Torres D.F., Romero G.E., Dame T., Combi J., Butt Y. M., & Aharonian F. 2002b, In preparation
- Totani T., & Kitayama T. 2000, *ApJ* 545, 572
- Véron-Cetty M.-P., & Véron P., 2001, *A&A* 374, 92
- von Montigny C., et al. 1995, *ApJ* 440, 525
- Wambsganss J., & Paczyński B. 1991, *ApJ* 102, 864
- Wambsganss J., & Paczyński B. 1994, *ApJ* 108, 1156
- Wambsganss J. 1999, *Jour. Comp. Appl. Math.* 109, 353
- Wambsganss J. 2001, in: *Proc. of the XXth Moriond Astrophysics Meeting "Cosmological Physics with Gravitational Lensing"*, eds. J.-P. Kneib, Y. Mellier, M. Moniez & J. Tran Thanh Van, p. 89; (also available as preprint astro-ph/0010004)
- Wilkind T., Combes F. 1996, *Nature* 379, 139
- Williams L.L.R., & Wijers, R.A.M.J. 1997, *MNRAS* 286, L11
- Witt H.J., & Mao S. 1994, *ApJ* 429, 66
- Wozniak P.R. et al. 2000, *ApJ* 540, L65
- Wyithe S., Turner E. L. 2002, *ApJ* 567, 18
- Zhang L., Zhang Y.J., & Cheng K.S. 2000, *A&A*, 357, 957

This figure "magpat_k50_g00.gif" is available in "gif" format from:

<http://arxiv.org/ps/astro-ph/0205441v1>

This figure "magpat_k80_g00.gif" is available in "gif" format from:

<http://arxiv.org/ps/astro-ph/0205441v1>

This figure "magpat_k20_g16.gif" is available in "gif" format from:

<http://arxiv.org/ps/astro-ph/0205441v1>

This figure "magpat_k90_g40.gif" is available in "gif" format from:

<http://arxiv.org/ps/astro-ph/0205441v1>